JOINT INSTITUTE FOR AERONAUTICS AND ACOUSTICS

National Aeronautics and
Space Administration

Ames Research Center

JIAA TR - 99

Stanford University

A Numerical Study Of The Effects Of Wind Tunnel Wall Proximity On An Airfoil Model

By

Mark Potsdam and Leonard Roberts

Stanford University
Department of Aeronautics and Astronautics
Stanford, CA 94305

September 1990

Abstract

A procedure has been developed for modeling wind tunnel flows using computational fluid dynamics. Using this method, a numerical study has been undertaken to explore the effects of solid wind tunnel wall proximity and Reynolds number on a two-dimensional airfoil model at low speed. Wind tunnel walls are located at varying wind tunnel height to airfoil chord ratios and the results are compared with freestream flow in the absence of wind tunnel walls. Discrepancies between the constrained and unconstrained flows can be attributed to the presence of the walls. Results are for a Mach Number of 0.25 at angles of attack through stall. A typical wind tunnel Reynolds number of 1,200,000 and full-scale flight Reynolds number of 6,000,000 were investigated. At this low Mach number, wind tunnel wall corrections to Mach number and angle of attack are supported. Reynolds number effects are seen to be a consideration in wind tunnel testing and wall interference correction methods.

The study uses an unstructured grid Navier-Stokes code with Baldwin-Lomax turbulence model. The numerical method is described since unstructured flow solvers present several difficulties and fundamental differences from structured grid codes, especially in the area of turbulence modeling and grid generation.

Acknowledgements

This work was performed under Boeing contract Y429804-0957N and NASA contract NCC2-055. Their support is gratefully acknowledged. I would like to thank Tim Barth and Marshal Merriam at NASA-Ames for the use of their flow solver and grid generation codes as well as numerous helpful discussions.

Contents

List of Tables

List of Figures

Nomenclature

A	Area
c	airfoil chord, 8 in.
c	speed of sound
C_d	drag coefficient, $\frac{D}{\frac{1}{2}\rho_\infty u_\infty^2 c}$
$C_{d_{press}}$	pressure or form drag coefficient
$C_{d_{visc}}$	viscous drag coefficient
C_f	skin friction coefficient, $\frac{\tau_{wall}}{\frac{1}{2}\rho_\infty u_\infty^2}$
C_l	lift coefficient, $\frac{L}{\frac{1}{2}\rho_\infty u_\infty^2 c}$
C_p	pressure coefficient, $\frac{p}{\frac{1}{2}\rho_\infty u_\infty^2}$
e	energy
$\mathbf{F}, \mathbf{G}$	Cartesian flux vectors
h/c	total wind tunnel height to airfoil chord ratio
i	cell index
j	node index
k	coefficient of thermal conductivity
ℓ	turbulent mixing length
M	Mach number
n	time index
n, t	normal, tangential coordinates
p	static pressure
PE	potential energy
$\mathbf{Q}$	vector of conserved variables (mass, momentum, energy)
R_1, R_2	Riemann invariants

R	residual
Re	Reynolds number, $\rho_\infty u_\infty c/\mu_\infty$
s	entropy
S	length
t	time
T	static temperature
u, v	Cartesian velocity components
u_τ	friction velocity, $\sqrt{\tau_{wall}/\rho_{wall}}$
x, y	Cartesian coordinates
y^+	turbulent law of the wall nondimensional normal coordinate, $u_\tau y/\nu_{wall}$
α	angle of attack, degrees
γ	ratio of specific heats, 1.4
θ	angle between adjacent edges
λ	second coefficient of viscosity, $-2/3\mu$
μ	coefficient of viscosity
μ_t	turbulent eddy viscosity
ν	kinematic viscosity, μ/ρ
ρ	density
τ	viscous shear stress
ω	vorticity, $\frac{\partial u}{\partial y} - \frac{\partial v}{\partial x}$
Ω	control volume with boundary $\partial\Omega$

Subscripts

e	Euler, inviscid
L,R	states on either side of an edge (left, right)
n, t	normal, tangential components
v	viscous
x, y	Cartesian derivatives, components
∞	freestream value

Chapter 1

Introduction

This work describes a procedure which has been developed for modeling wind tunnel flows using computational fluid dynamics (CFD). Possible applications of the CFD code, grid generation programs, and boundary conditions discussed here are numerous. Results of a fundamental study of the effects of solid wind tunnel wall proximity and Reynolds number on an airfoil model are presented.

1.1 Applications

CFD validation benefits from the ability to numerically calculate wind tunnel flows. When wind tunnel walls are simulated directly, the errors due to wind tunnel wall interference correction methods are eliminated. This enables a direct comparison of experimental data with computational results. With the effects of the wall correction method removed, discrepancies can more accurately be attributed to numerical errors. This idea is promising for the validation of turbulence models in that it can pinpoint areas of weakness in the model. Errors due to the simulation of porous or slotted walls can be eliminated if solid walls are used.

A broad range of flow regimes can be handled more expediently with a CFD code than with experimental tests. The numerical simulation also provides considerably more data than is available from wind tunnel tests. Alternatively, CFD simulations

can be used for the development of wind tunnel wall interference correction methods. The computational data can determine the effects which must be included in a correction method and the appropriateness of a particular method. Although wind tunnel wall interference assessment/correction (WIAC) techniques have made considerable progress and are often quite reliable, numerous issues must still be addressed in future developments [1, 2]. Reynolds number effects are an important area which can be investigated using a Navier-Stokes code. For CFD validation methods and wind tunnel wall interference correction methods which employ wind tunnel measurements directly, the large amount of data available from CFD analyses can be used to determine the amount and location of experimental data that is required so that experimental measurements will be minimized. CFD codes are often used as part of WIAC methods to determine effective airfoil shapes and to iterate on Mach number and angle of attack corrections [1].

Although the eventual aim of a wind tunnel experiment is to be able to relate it to full-scale free flight, understanding of both flow conditions is necessary. The CFD code and grid generation system developed here allow for studies of Reynolds number effects; solid, porous, and slotted wall effects; wall proximity effects; laminar versus turbulent effects; as well as the modeling of a wide range of geometries, angles of attack, and flow conditions.

1.2 Current Configuration

The code was used in this work to study the effects of wind tunnel wall proximity and Reynolds number on a two-dimensional single element airfoil model at low speed. Wind tunnel wall proximity effects are important because it is desirable to put as large a model in a wind tunnel as possible. Conversely, small wind tunnels are more economical to operate. Larger models are not only easier to build and instrument, but they more closely match full-scale Reynolds numbers. Reynolds number and wall proximity effects are coupled in that attempts to duplicate higher Reynolds numbers are often limited by blockage effects due to wall proximity.

The computations in this work use a Boeing advanced transport research airfoil.

The airfoil has camber. Although the model includes a main airfoil and flap, the flap has been retracted for this study. Four angles of attack were computed: $\alpha = 0$, 5, 10, and 15 degrees. The first three cases yield attached flow while at fifteen degrees the airfoil is mostly separated.

Solid wall wind tunnel flows were computed with total height to airfoil chord ratios of 1.5, 2.25, 4.5 and ∞ (unconstrained). The unconstrained case sets the outer boundary 12 chords away from the airfoil. For conformity with the wind tunnel cases, the grid for the unconstrained case can be equated to a height to chord ratio of 24, although the boundary conditions are different. The wind tunnel inflow plane was located five chords upstream from the leading edge and the exit is fifteen chords downstream from the leading edge. The wind tunnel walls were modeled as solid.

The flow is at a freestream Mach number of 0.25. Two Reynolds numbers based on the airfoil chord were considered: 1,200,000 and 6,000,000. A Reynolds number of 1,200,000 is typical of a low speed wind tunnel as is a height to chord ratio of 2.25. This configuration is patterned after experimental work done on the airfoil with flap extended at the Stanford subsonic wind tunnel [3]. Full-scale testing is simulated by the higher Reynolds number.

The CFD code is an unstructured grid Navier-Stokes solver with a Baldwin-Lomax algebraic turbulence model. The Reynolds-averaged Navier-Stokes equations are solved so that viscous phenomenon, most importantly the wake and boundary layer, can be included and investigated. Reynolds number effects have been shown to affect airfoil characteristics and the level of wall interference [2]. A turbulence model is used because the flows studied here are typically turbulent. In the wind tunnel, transition occurs naturally or the boundary layer is artificially tripped to simulate full-scale conditions.

A major advantage of an unstructured grid is its flexibility in modeling complex geometries. The single element airfoil investigated here is a precursor to future work on a multielement model for which an unstructured grid is well suited, although turbulence modeling can become more complex. The grid generation scheme is demonstrated using a multielement airfoil and wind tunnel configuration. Another benefit of using unstructured grids is the ease with which they can be refined and adapted

to resolve flow features. Currently, to obtain the benefits of using unstructured grids, while removing the penalties of structured grids, extra steps are required in the grid generation process. The computational method will be discussed along with the appropriate boundary conditions for wind tunnel flows, particularly for the inflow and outflow planes.

Chapter 2

Computational Method

The computational fluid dynamics code solves the Navier-Stokes equations in conservative form on an unstructured grid in two dimensions. The space derivatives are discretized using a finite volume formulation which is employed up to the boundaries. Roe's flux difference splitting is used for the inviscid terms and central differencing is used for the viscous terms. The Baldwin-Lomax algebraic turbulence model is implemented. Because of the unstructured grid, explicit time stepping is used to advance the solution to steady state. Several enhancements are added to speed convergence. The code was developed by Timothy Barth at NASA-Ames Research Center. See Reference 4 for details and further references.

2.1 Equations

The Navier-Stokes equations in differential conservative form are

$$\frac{\partial \mathbf{Q}}{\partial t} + \frac{\partial \mathbf{F_e}}{\partial x} + \frac{\partial \mathbf{G_e}}{\partial y} = \frac{\partial \mathbf{F_v}}{\partial x} + \frac{\partial \mathbf{G_v}}{\partial y} \tag{1}$$

where,

$$\begin{aligned} \mathbf{Q} &= [\rho, \rho u, \rho v, e]^T \\ \mathbf{F_e} &= \left[\rho u, \rho u^2 + p, \rho uv, u(e+p)\right]^T \\ \mathbf{G_e} &= \left[\rho v, \rho uv, \rho v^2 + p, v(e+p)\right]^T \end{aligned}$$

$$
\begin{aligned}
\mathbf{F_v} &= [0, \tau_{xx}, \tau_{xy}, u\tau_{xx} + v\tau_{xy} + kT_x]^T \\
\mathbf{G_v} &= [0, \tau_{yx}, \tau_{yy}, u\tau_{yx} + v\tau_{yy} + kT_y]^T \\
\tau_{xx} &= 2\mu u_x - \lambda(u_x + v_y) \\
\tau_{xy} = \tau_{yx} &= \mu(u_y + v_x) \\
\tau_{yy} &= 2\mu v_y - \lambda(u_x + v_y)
\end{aligned}
$$

In integral form they are written

$$\int_\Omega \frac{\partial \mathbf{Q}}{\partial t}\, dA + \int_\Omega \left(\frac{\partial \mathbf{F_e}}{\partial x} + \frac{\partial \mathbf{G_e}}{\partial y} \right) dA = \int_\Omega \left(\frac{\partial \mathbf{F_v}}{\partial x} + \frac{\partial \mathbf{G_v}}{\partial y} \right) dA \tag{2}$$

where Ω represents a control volume with differential area dA. The area integrals can be converted to surface integrals over the boundary of Ω, resulting in a flux balance over the control volume:

$$\frac{\partial}{\partial t} \int_\Omega \mathbf{Q}\, dA + \int_{\partial\Omega} (n_x \mathbf{F_e} + n_y \mathbf{G_e})\, dS = \int_{\partial\Omega} (n_x \mathbf{F_v} + n_y \mathbf{G_v})\, dS \tag{3}$$

where dS is a differential length on the boundary $\partial\Omega$ and n_x and n_y are the unit normals to the boundary.

2.2 Discretization

The finite volume formulation used here discretizes the control volume as a polygon so that the integration becomes a numerical quadrature over the discrete faces of the polygon:

$$\frac{d\bar{\mathbf{Q}}_\mathbf{j}}{dt} + A_j^{-1} \sum_{i=1}^{nfaces(j)} [n_x(\mathbf{F_e} - \mathbf{F_v}) + n_y(\mathbf{G_e} - \mathbf{G_v})]\, \Delta S_i = 0 \tag{4}$$

Arbitrary polygons are handled in this manner. The term in brackets in Equation 4 is the oriented flux along the i^{th} edge of the control volume with length ΔS_i. The vector of conserved variables $\bar{\mathbf{Q}}$ at node j is the cell averaged data such that

$$\bar{\mathbf{Q}}_\mathbf{j} = A_j^{-1} \int_{\Omega_j} \mathbf{Q}\, dA \tag{5}$$

The flow variables are, therefore, piecewise constant in each cell. Data is stored at the vertices of the mesh, and the median dual mesh is used as the control volumes.

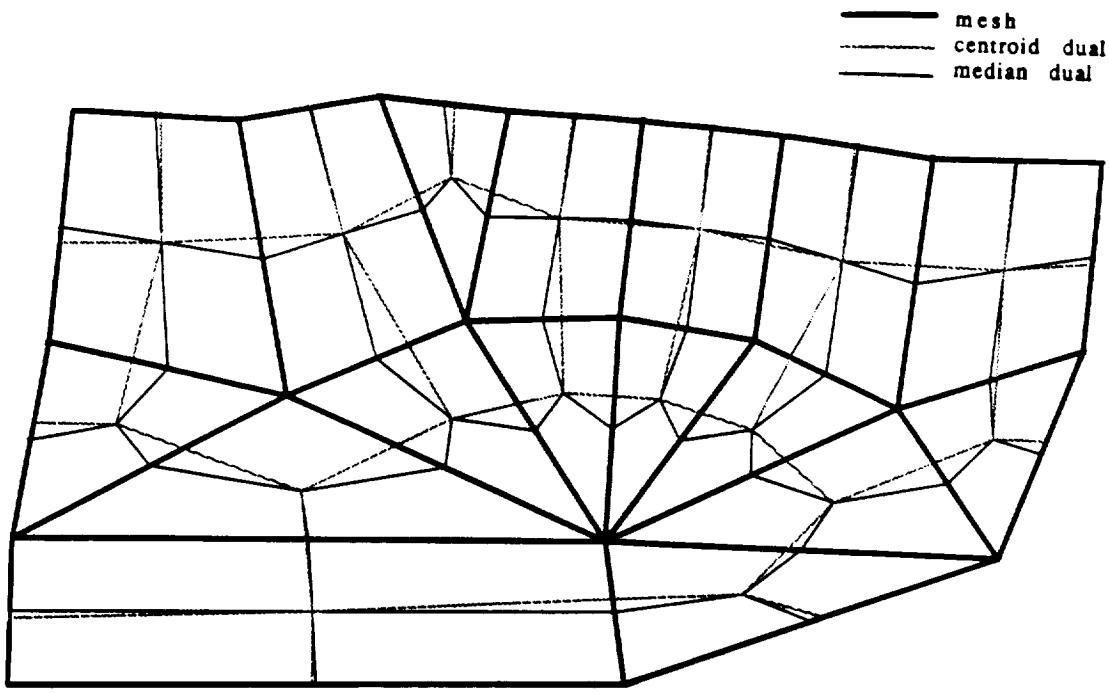

Figure 1: Mesh Geometry and Control Volumes

The median dual is formed by connecting cell centroids to edge centers as shown in Figure 1. Currently, the grid cells are either triangles or quadrilaterals. The numerical integration is done over all discrete segments of the control volume for better accuracy at triangle/quadrilateral cell interfaces. This is necessary because the difference in truncation error between the two cell geometries causes accuracy problems. This improved quadrature adds additional computational time.

2.3 Fluxes

The inviscid fluxes are computed using Roe's flux difference splitting. Rewriting Equation 4, the oriented flux, $\mathbf{f_n}$, is considered to be a function of the states on either

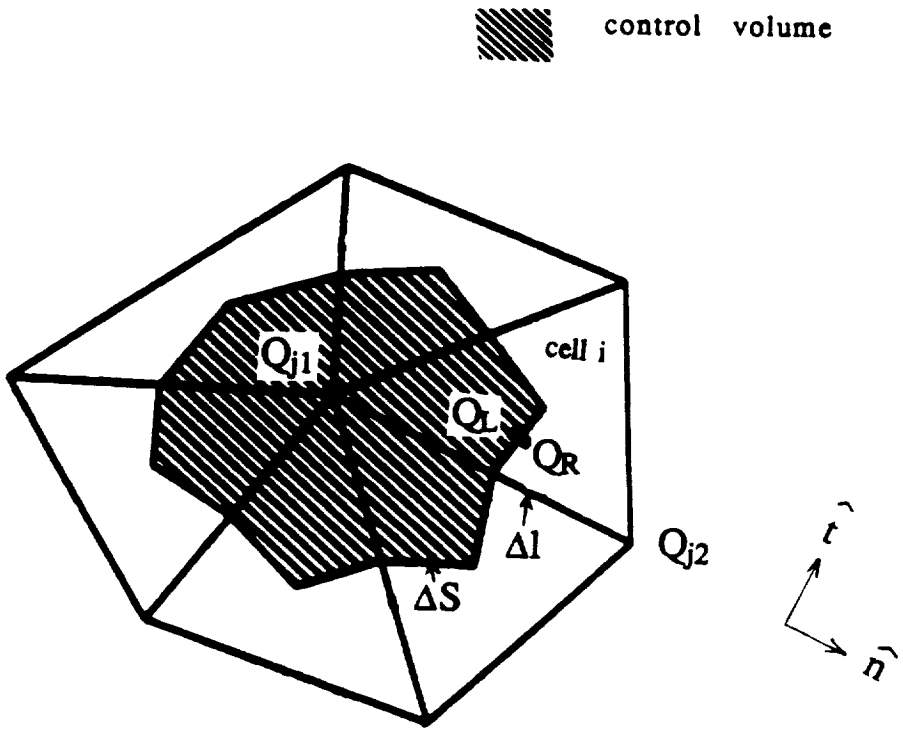

Figure 2: Control Volume and Variables

side of an edge of the control volume, $\mathbf{Q_L}$ and $\mathbf{Q_R}$ (Figure 2):

$$\frac{d\bar{\mathbf{Q}}_\mathbf{j}}{dt} + A_j^{-1} \sum_{i=1}^{nfaces(j)} \mathbf{f_n}(\mathbf{Q_L}, \mathbf{Q_R})\, \Delta S_i = 0 \tag{6}$$

Roe's flux function defines the oriented flux to be an approximate solution to the Riemann problem at this edge:

$$\mathbf{f_n}(\mathbf{Q_L}, \mathbf{Q_R}) = \frac{1}{2}\left[\mathbf{f_n}(\mathbf{Q_L}) + \mathbf{f_n}(\mathbf{Q_R})\right] - \frac{1}{2}|A(\mathbf{Q_L}, \mathbf{Q_R})|\,(\mathbf{Q_L} - \mathbf{Q_R}) \tag{7}$$

The first term represents a standard central difference while the second term adds an upwind influence by distinguishing incoming and outgoing waves. This term also has the effect of adding artificial dissipation to stabilize the solution. The matrix A is the Jacobian matrix of $\mathbf{f}$, $\partial \mathbf{f}/\partial \mathbf{Q}$. The matrix $|A|$ has the same eigenvectors as A, but its

eigenvalues are the absolute value of those of A. $\mathbf{Q_L}$ and $\mathbf{Q_R}$ determine the order of accuracy of the scheme and are defined in the next section.

In the viscous fluxes the values of the conservative variables at an edge of the control volume are an average of the nodal values on either side of the edge. The gradients in the viscous fluxes there are computed similar to a finite difference formulation using the values $\mathbf{Q_{j1}}$ and $\mathbf{Q_{j2}}$ (Figure 2). In addition to the gradient component along the $j1$–$j2$ edge, the perpendicular component of the gradient in cell i is added:

$$\nabla \mathbf{Q_v} = \frac{\mathbf{Q_{j2}} - \mathbf{Q_{j1}}}{\Delta l} \hat{\mathbf{n}} + \nabla \mathbf{Q_{t_i}} \hat{\mathbf{t}} \tag{8}$$

2.4 Higher Order Accuracy

A first order scheme is created if $\mathbf{Q_L}$ and $\mathbf{Q_R}$ in the inviscid fluxes are taken as nodal values. A higher order scheme is created if the cell averaged nodal data is reconstructed to be piecewise linear in a cell rather than assumed constant. In the piecewise linear case, $\mathbf{Q_L}$ and $\mathbf{Q_R}$ at an edge of the control volume are determined from an expansion about nodal data:

$$\mathbf{Q_L} = \mathbf{Q_j} + \nabla \mathbf{Q_j} \cdot \Delta \mathbf{r} \tag{9}$$

where $\mathbf{Q_j}$ and $\nabla \mathbf{Q_j}$ are the nodal data and gradients and $\Delta \mathbf{r}$ is the vector between the node and the midpoint of an edge of the control volume as seen in Figure 3. The nodal gradients used in reconstruction are computed from:

$$\int_\Omega \nabla \mathbf{Q}\, dA = \oint_{\partial\Omega} \mathbf{Q}\, \hat{\mathbf{n}}\, ds \tag{10}$$

With linear reconstruction $\nabla \mathbf{Q}$ is constant so that

$$\nabla \mathbf{Q_j} = A_j^{-1} \oint_{\partial\Omega} \mathbf{Q}\, \hat{\mathbf{n}}\, ds \tag{11}$$

Using a path of integration made up of the surrounding cells as in Figure 3, the nodal gradient is computed as

$$\nabla \mathbf{Q_j} = A_j^{-1} \sum_{i=1}^{nfaces(j)} \mathbf{Q_i}\, \hat{\mathbf{n}}_i\, \Delta s \tag{12}$$

The cell gradients, $\nabla \mathbf{Q_i}$, used in the viscous fluxes are computed in a similar manner using the cell boundary as the contour of integration.

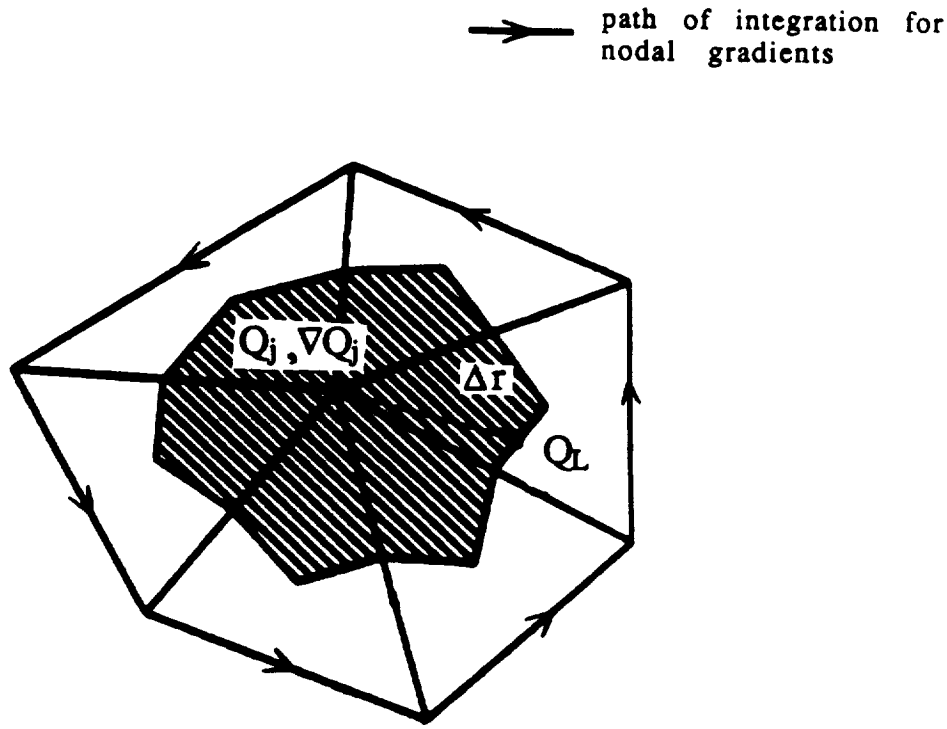

Figure 3: Higher Order Accuracy, Nodal Gradient Calculation

2.5 Turbulence Modeling

Barth has implemented the Baldwin-Lomax algebraic turbulence model [5] in the code. The effects of turbulence are modeled by the addition of a turbulent eddy viscosity to the molecular viscosity in the viscous stresses. This requires special procedures to be executed on an unstructured grid.

2.5.1 Baldwin-Lomax Model

The two layer model is defined as follows. In the inner layer:

$$\mu_{t_{inner}} = \rho \ell^2 |\omega| \tag{13}$$

where,

$$\ell = ky\,[1 - e^{-y^+/A^+}]$$

is the turbulent mixing length. In the outer layer:

$$\mu_{t_{outer}} = KC_{CP}\rho F_{wake} F_{Kleb}(y) \tag{14}$$

where,

$$\begin{aligned} F_{wake} &= \min(y_{max}F_{max}, C_{WK}y_{max}U_{diff}^2/F_{max}) \\ F(y) &= y|\omega|[1 - e^{-y^+/A^+}] \\ F_{Kleb} &= \left[1 + 5.5\left(\frac{C_{Kleb}y}{y_{max}}\right)^6\right]^{-1} \\ U_{diff} &= u_{max} - u_{min} \end{aligned}$$

The constants k, A^+, K, C_{CP}, C_{WK}, and C_{Kleb} are those defined in the original paper by Baldwin and Lomax [5]. The coordinate direction y is actually the normal distance from the wall and is not always aligned with the Cartesian direction. The crossover point from inner to outer layer is determined by the location where $\mu_{t_{inner}}$ exceeds $\mu_{t_{outer}}$ in a profile. The quantity F is the damped moment of vorticity, and the location of its maximum in a boundary layer or wake profile is used as a length scale to compute turbulent viscosity. In structured meshes it is a simple procedure to

scan boundary layer or wake profiles to find this maximum because the profiles are typically coordinate lines normal to the body or wake centerline. In an unstructured grid, these lines may exist, especially if the unstructured grid was generated from a structured one, but they are not easily accessed since unstructured meshes have no preferred set of coordinate directions.

2.5.2 Implementation on Unstructured Grids

The current implementation constructs these lines using geometry information from only the boundary edges and points. The procedure for near wall flows is as follows: For each grid point find the nearest no slip boundary edge, the distance to the nearest point on this boundary edge, and an interpolation factor based on the location of this nearest point on the boundary edge. The interpolation factor is used to determine which boundary edge endpoint is referenced and to interpolate to the normal line represented by this endpoint. The trailing edge point is marked and all points which have this point as the closest are flagged as wake points. A mixing length model is used in the wake. All points which reference a particular boundary point as closest are considered to be in that point's boundary layer profile. The points are sorted in order of increasing distance from the body in a preprocessing stage.

At each time step the moment of vorticity, F, and the inner layer turbulent viscosity are computed for all points. The points are then processed in sorted order to find the maximum moment of vorticity, F_{max}, for each boundary layer profile and, therefore, each boundary point. This is possible since the interior points where the function is computed all reference a boundary point. The value of the function in the field is used in conjunction with the interpolation factor to compute properties at specific boundary stations. The outer layer turbulent viscosity for each interior point is calculated as a function of the distance of the point from the wall and F_{max} of the referenced boundary point. Finally, the points are again processed in sorted order to find the crossover point from inner to outer layer for each profile. No transition model is implemented, but this is not a limitation of the unstructured grid.

The method works particularly well when the unstructured mesh is originally obtained from a structured mesh and lines normal to the body do exist. If the grid is

completely unstructured the current implementation can break down. This happens when a boundary point cannot generate a complete set of points which span the entire profile. An incorrect length scale can be computed because the boundary point does not see the outer edge of the layer. A more robust implementation would have boundary points pointing to field points to make up a profile rather than field points pointing to boundary points. Rostand [6] does this by generating normal lines at each boundary point and storing the interior edges and points which the profile intersects. All interior points then use boundary normal lines to interpolate from. An alternative method for creating boundary normals is to employ background structured grids and interpolate flow variables and turbulence quantities back and forth, but this can be quite memory intensive [7]. No problems were encountered with the current method since the grids had some original structure to them, and when boundary points were added, care was taken to add a complete profile to go with them.

The process of setting up the nearest boundary edges and points as well as the sorting is only performed once because this information is stored. Storage required for the turbulence model is two real arrays: 1) the distance to the nearest wall and 2) the interpolation factor, and two integer arrays: 1) the referenced boundary edge and 2) the order of sorted points. All of these arrays have dimensions of the number of nodes in the mesh. These arrays are the only additional storage requirements due to the unstructured nature of the grid. The Baldwin-Lomax model requires the storage of the maximum moment of vorticity and its location as well as inner and outer turbulent viscosities, but these arrays represent no additional storage because previously dimensioned arrays are reused for these variables. The current method uses less than 5% of the total memory requirements.

2.5.3 Considerations for Complex Flows

Confluent or overlying shear layers which are present in multielement airfoil flowfields are currently not handled correctly. When using an algebraic model, the boundary layer of the flap must have a different length scale than the overlying main element wake. This is not accounted for as the the current implementation only creates one

length scale per profile. If an algebraic model is used several alternatives can be proposed to treat the interaction of turbulent wakes and boundary layers. Mavriplis [7] has implemented the aforementioned method of background structured grids and has shown impressive results for a four element airfoil. Alternatively, with minor modifications to the current method, wake edges can be included in the list of boundary edges. The turbulence model will then perform in a manner similar to structured grid implementations which use a grid line approximating the wake centerline. When adjacent boundary layers and wakes start to merge, a combination of turbulent viscosities is required.

For complex flows such as confluent wakes, algebraic turbulence models are probably no longer reliable. Execution of a one or two-equation model such as k-ϵ presents little difficulty on an unstructured mesh. One of the major disadvantages is the time required to integrate another, possibly stiff, equation. A modified k-ϵ model has performed reasonably for merging and confluent wakes and boundary layers [8].

2.6 Time Evolution

The time derivative in Equation 6 is discretized using an explicit 3 stage Runge-Kutta time stepping scheme. For the finite volume space discretization:

$$\begin{aligned}
\mathbf{Q_j}^{(0)} &= \mathbf{Q_j}^{(n)} \\
\mathbf{Q_j}^{(1)} &= \mathbf{Q_j}^{(0)} - C_1 \frac{dt_{max_j}}{Vol_j} \mathbf{R_j}(\mathbf{Q_j}^{(0)}) \\
\mathbf{Q_j}^{(2)} &= \mathbf{Q_j}^{(0)} - C_2 \frac{dt_{max_j}}{Vol_j} \mathbf{R_j}(\mathbf{Q_j}^{(1)}) \\
\mathbf{Q_j}^{(3)} &= \mathbf{Q_j}^{(0)} - C_3 \frac{dt_{max_j}}{Vol_j} \mathbf{R_j}(\mathbf{Q_j}^{(2)}) \\
\mathbf{Q_j}^{(n+1)} &= \mathbf{Q_j}^{(3)}
\end{aligned} \tag{15}$$

$$C_1 = .18, \qquad C_2 = .5, \qquad C_3 = 1.0$$

To accelerate convergence local time stepping is used. The time step in each cell is determined by the local CFL number in that cell and, therefore, varies throughout the mesh. The calculation is no longer time accurate. The CFL number is computed

from monotonicity principles and is typically overrestrictive when compared with a conventional CFL number [4].

Another method used to speed convergence is grid sequencing. The solution is initially started on a coarse grid where the Euler equations are solved. This allows the solution which uses freestream initial conditions to set up rapidly. The viscous terms are then turned on to set up a boundary layer and wake. Grid adaption is used to refine the wake and boundary layer until the desired spacing is obtained. Examples of this procedure are given in the following section on grid generation

Chapter 3

Grid Generation

The major advantage in using unstructured grids is the inherent flexibility in treating complicated geometries. Complex flows can also be computed more easily and accurately using grid adaption. Extra effort, though, is required to obtain the unstructured grids suitable for viscous calculations.

3.1 Method

The method will be demonstrated to generate a fine mesh about a multielement airfoil in a wind tunnel. This configuration would be a difficult task for a structured grid generator. The first step in generating the unstructured grid involves generating structured grids about all components: main airfoil, flap, and wind tunnel [9]. The background wind tunnel grid is Cartesian while grids about the airfoils are body conforming C-meshes, best at resolving boundary layers and wakes. The grids are overlaid (Figure 4) and overlapping sections, for example, those which fall within a body, are removed (Figure 5). At this point quadrilateral cells in boundary layers and wakes can also be removed for later reinsertion into the unstructured grid. These large aspect ratio cells can cause problems in latter steps in the grid generation process. This sequence of steps is done interactively on a graphics workstation.

The connectivity of the points is thrown out, and only the coordinates of the points are saved. These points are then filtered. Points that were required in the initial grid

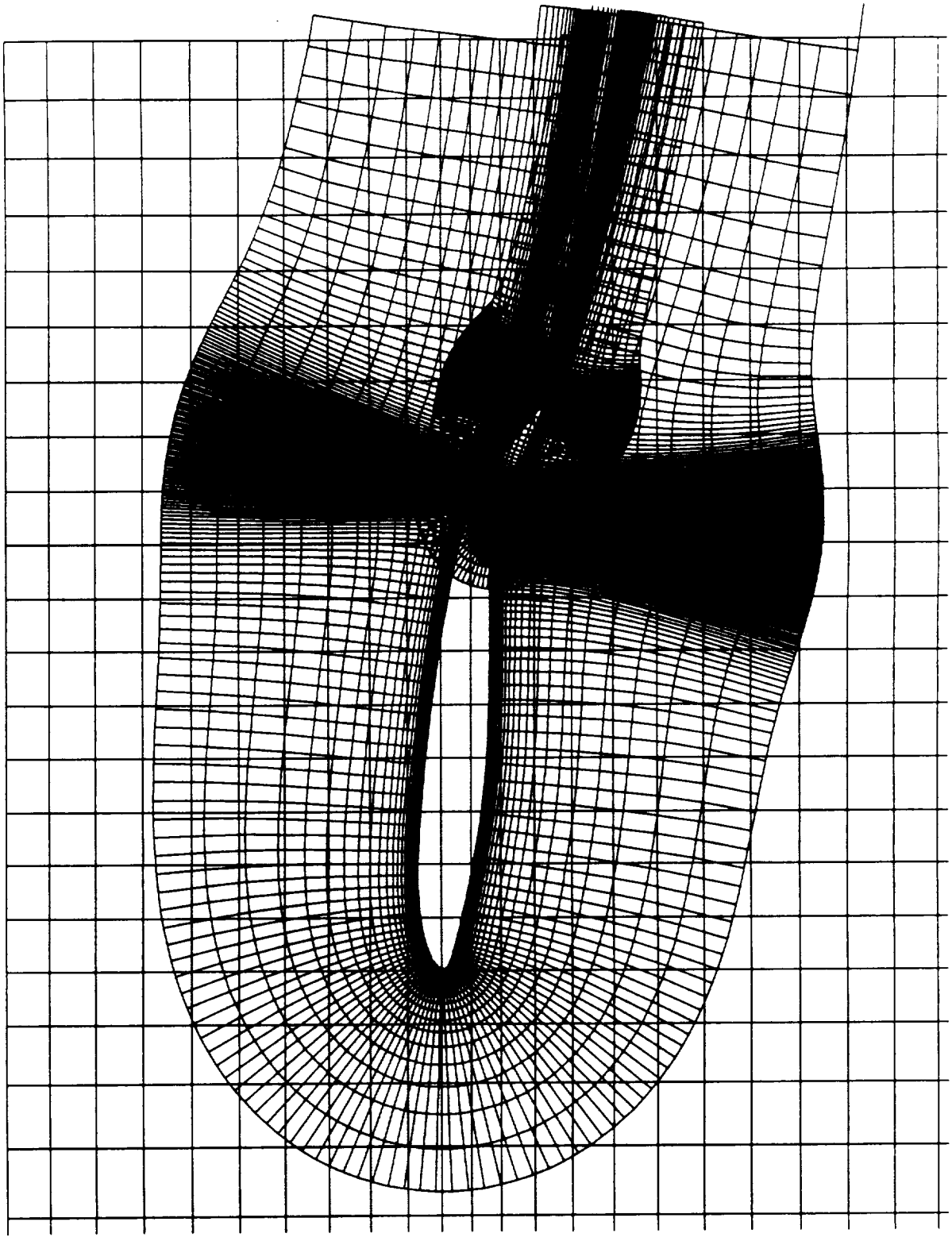

Figure 4: Overlaid Structured Grids

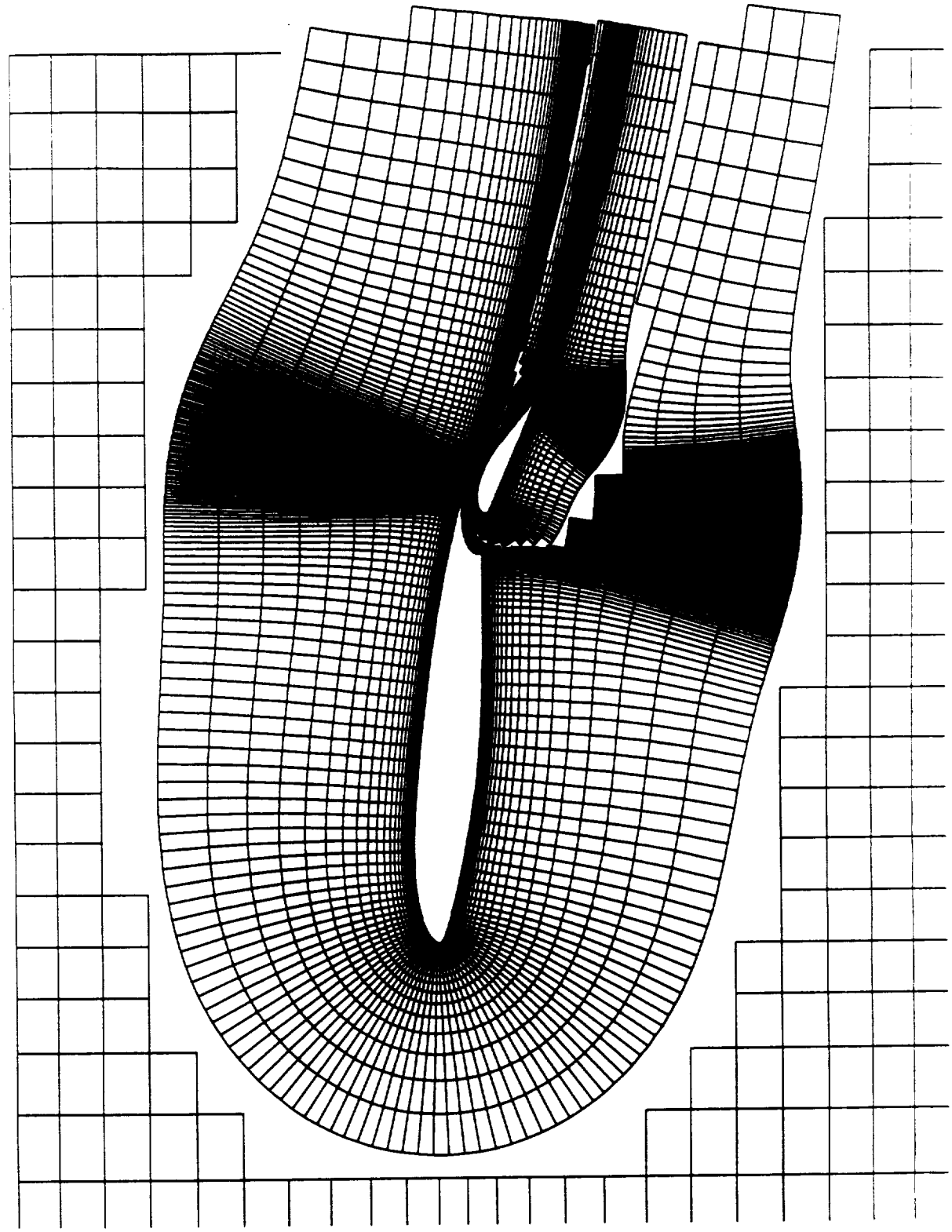

Figure 5: Overlapping Sections Removed from Structured Grids

due to its structured nature but which are not necessary for accuracy are discarded. For example, clustering at the trailing edge in a structured grid extends out into the field where it is not needed. By setting up a function in space which takes on the value of the minimum specified spacing between points, points are automatically filtered. Figure 6 illustrates the resulting cloud of points after such a filtering. The size of the crosses at the points indicates the minimum spacing between points. Note the points that have been removed around the airfoil when the boundary layer cells were saved. Points are also removed from the far downstream wake where they are not needed as the wake dies out (Figure 7).

The next step involves connecting the points using a Delauney triangulation algorithm [10] (Figure 8). A Delauney triangulation is constructed by making three points into a triangle if their circumcircle contains no other points. Another property of Delauney triangulation is that it maximizes the minimum angle in the mesh. The resulting grid is isotropic with no directional bias. This is not always optimal, especially for grids with high aspect ratio cells as is typically required for viscous calculations. Problems such as seen in Figures 8 and 9 can result when the triangulation does not recover the initial structured mesh. This is one of the reasons quadrilateral boundary layer cells are removed early in the process. Another reason is to help prevent edges from "breaking through" across a body.

In order to regain a directionally biased mesh, after the global triangulation is completed, the mesh is retriangulated locally in a stretched plane using an edge swapping algorithm [11]. The original structured grids give the information about the transformed plane, namely a stretching vector with magnitude and direction. The vector is associated with the aspect ratio and major axis of surrounding cells at a point. The maxmin angle property of Delauney triangulation is utilized locally by considering two triangles with a shared edge. The orientation of the shared edge is determined by satisfying the maxmin angle criterion in the stretched plane. Several iterations through the mesh result in edges being swapped into the desired configuration (Figure 10).

The mesh is now made up only of triangles. The next step involves removing diagonals to form quadrilaterals out of two adjacent triangles [10]. This recovers most

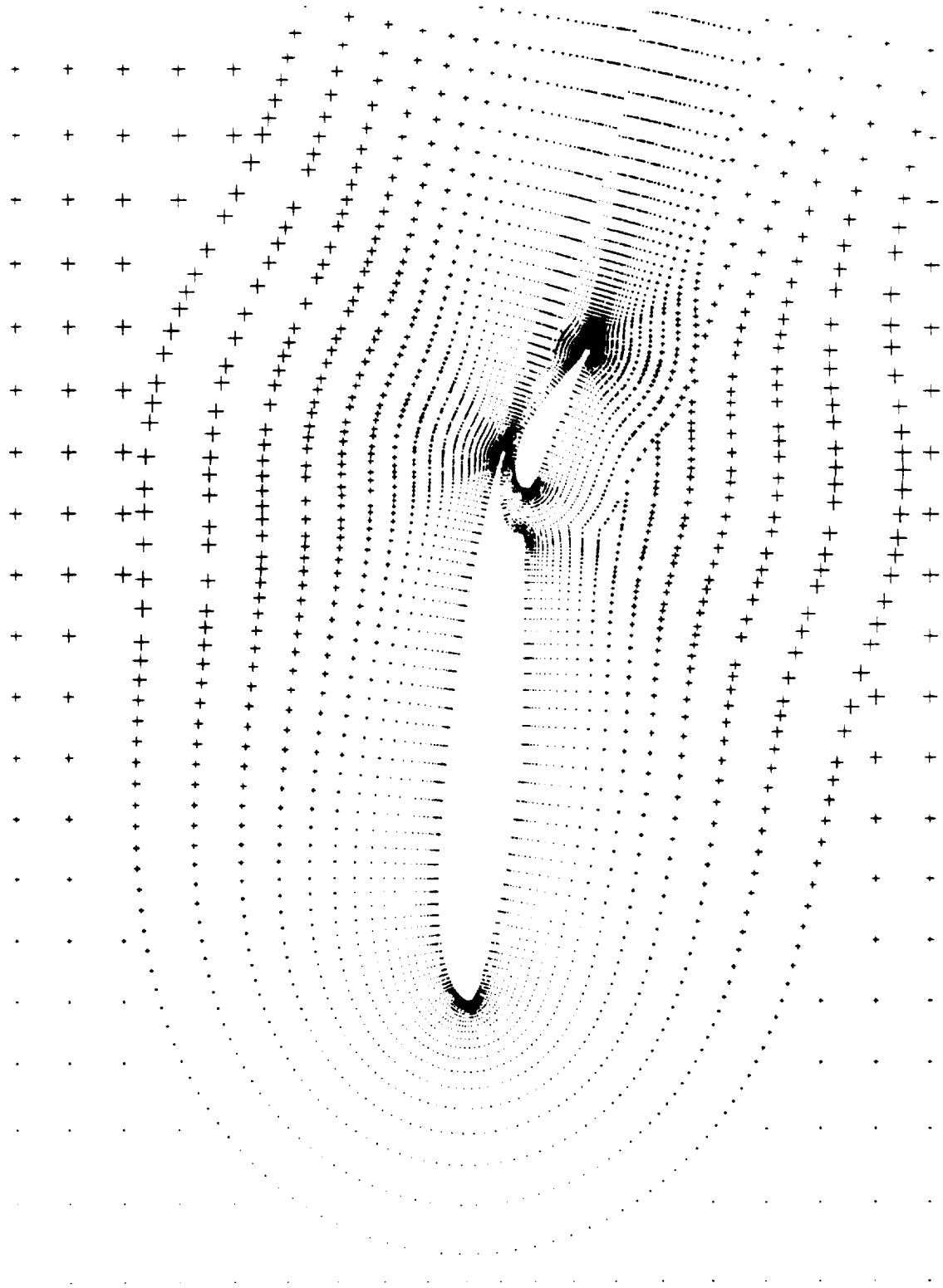

Figure 6: Filtered Points and Spacing Function

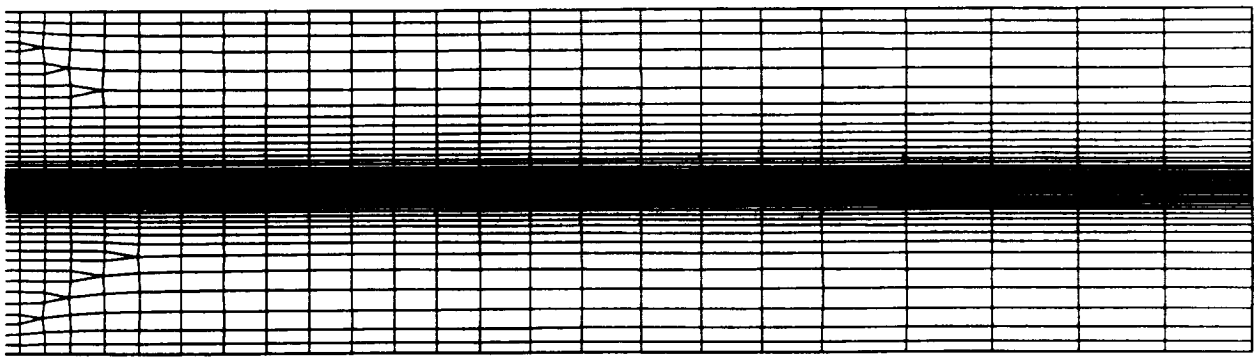

Figure 7: Filtered Points in the Wake

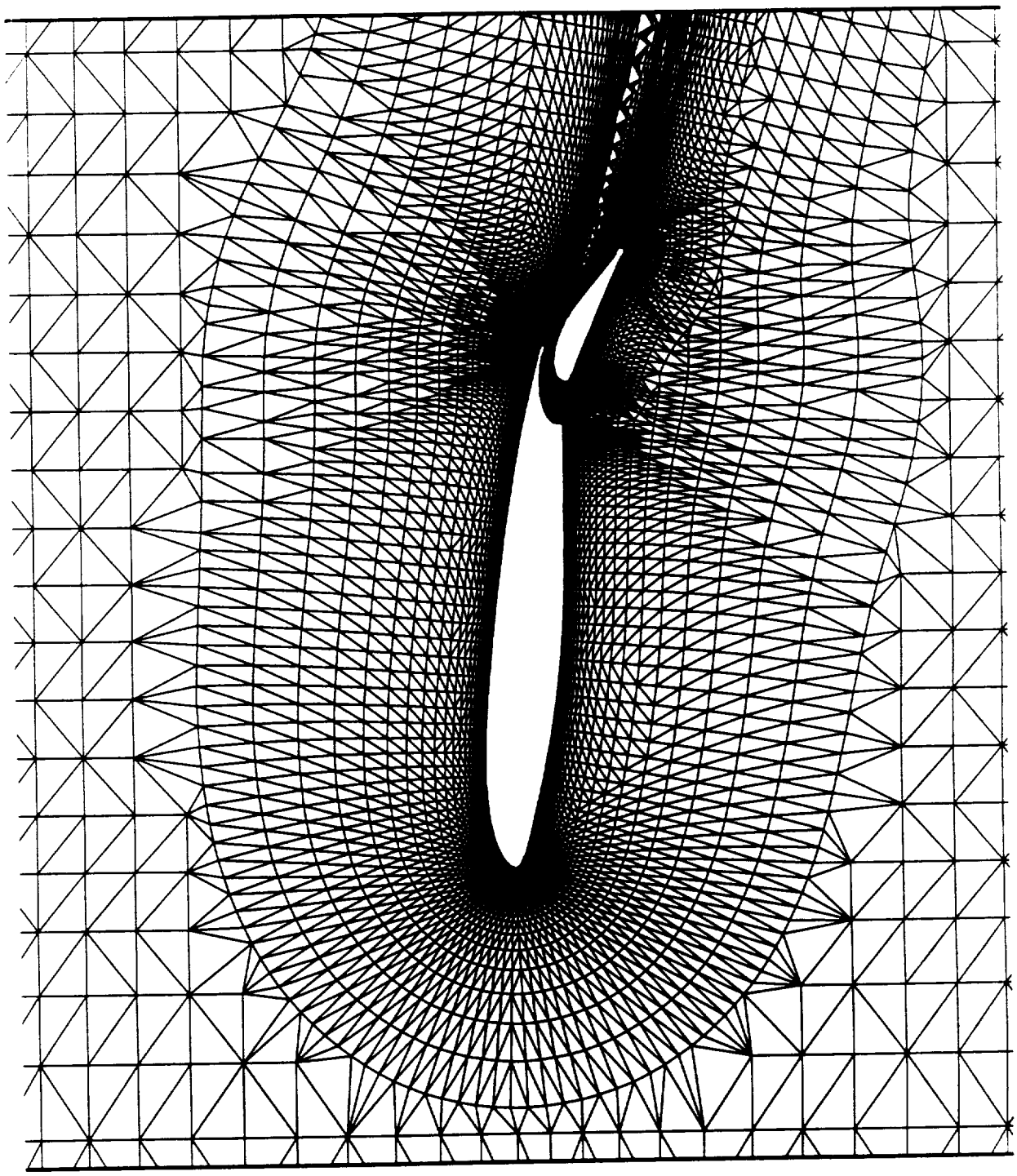

Figure 8: Delauney Triangulation

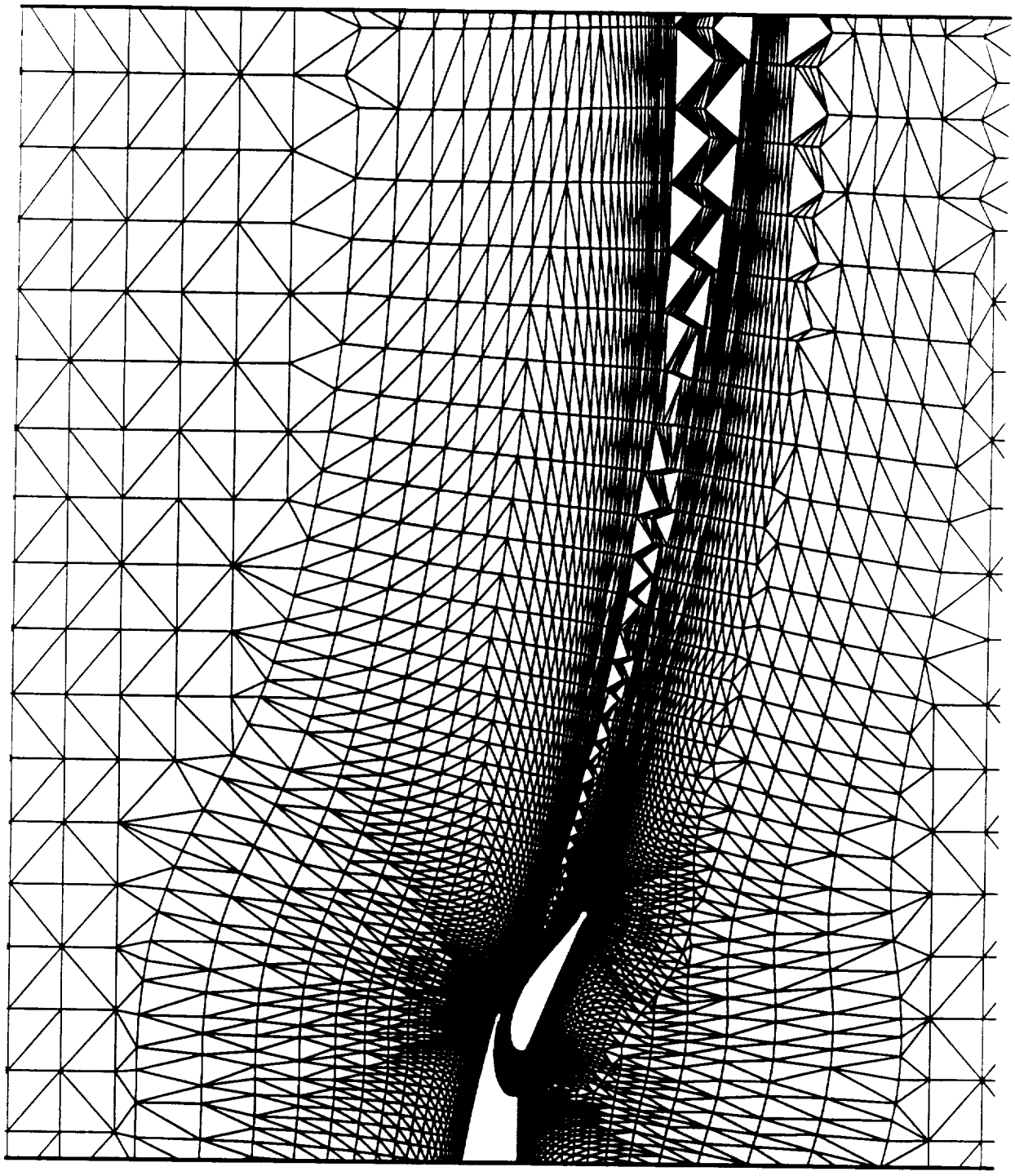

Figure 9: Non-Optimal Delauney Triangulation with Viscous Grids

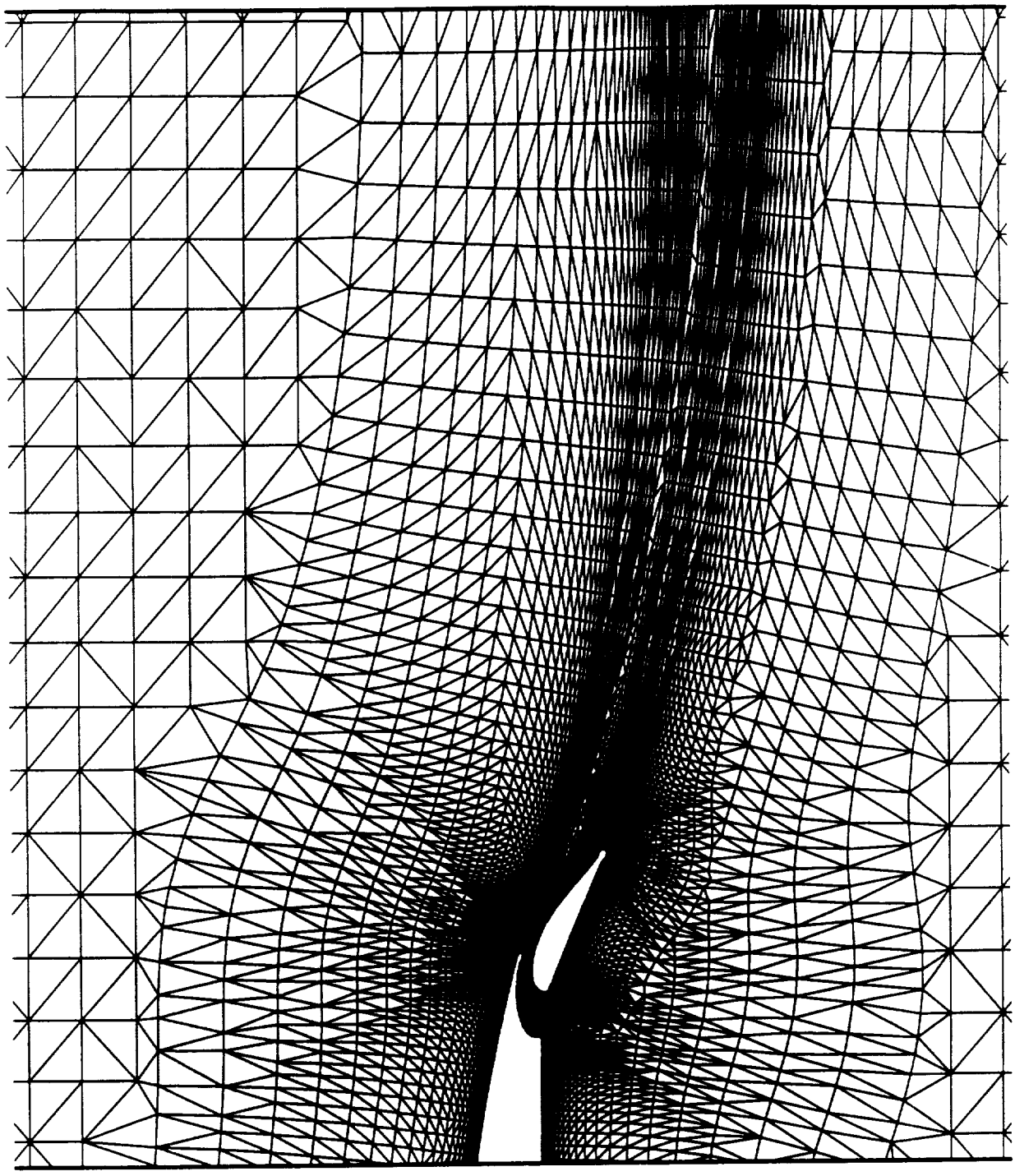

Figure 10: Edge Swapping in Locally Stretched Plane

of the structured grid that was not destroyed in the filtering process. At this point the boundary layer quadrilaterals are also merged back in (Figure 11). Quadrilaterals are used for several reasons. They work well in shear layers where triangles with small height to base ratios, which have edges that are not aligned with the flow gradients, need to be avoided. They are also more accurate than triangles. The flow code is edge based in that most operations are done in loops over edges. Quadrilateral cells reduce the number of edges thereby increasing speed and decreasing storage. Triangles are generally only used when it is necessary to transition between different mesh geometries, airfoil elements, or areas of grid refinement.

The last step in the mesh generation process, which can be seen in Figure 11, was to smooth the points. Near boundaries with high curvature, crossed grid lines can result if a simple Laplacian smoothing, *i.e.* averaging of surrounding coordinate values, is used. The procedure employed places torsion springs between adjacent edges of a vertex and approximately solves a local minimization of potential energy problem for each node with its surrounding cells. To prevent very small cells and large area variations, a term proportional to the inverse area of a cell is also added to the potential energy, which is computed as

$$PE(x_j, y_j) = \sum_{i=1}^{nvertex(j)} \left[\frac{1}{2} \Delta\theta^2(x_j, y_j) - \frac{K}{A_i(x_j, y_j)} \right] \tag{16}$$

where $\Delta\theta$ is the angle between two adjacent edges, A_i is the enclosed area, and K is a constant equal to 0.3. The potential energy is minimized by solving for the coordinates of the vertex, x_j and y_j. Only a small number of smoothing sweeps are required. Extremely irregular geometries such as the trailing edges of viscous O-meshes can be smoothed with this method without underrelaxation.

3.2 Grid Adaption

A final issue to be addressed in the grid generation process is grid adaption. As mentioned earlier, the time required to reach a steady state on a grid of specified fineness can be sped up if major flow features are first resolved on a coarse grid and grid points are then added in the areas of high gradients only. In particular,

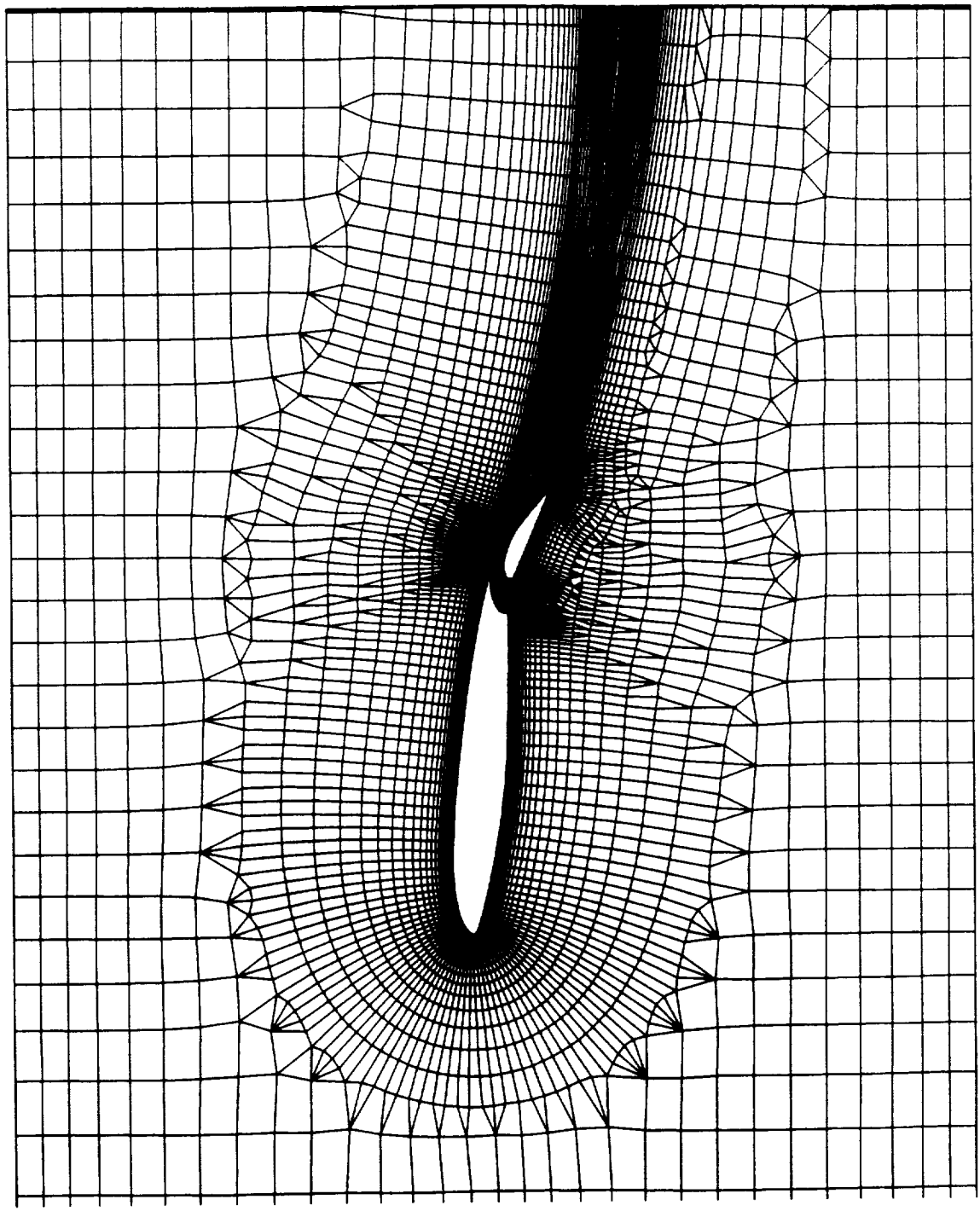

Figure 11: Final Grid - Quadrilaterals and Triangles

angle of attack (degrees)	0	5	10	15
nodes	11034	14880	13972	19595
cells (% triangles)	11599 (13)	15935 (8)	14601 (12)	21220 (18)
edges	22633	30275	28753	40815
points on the airfoil	197	274	281	368

Table 1: Grid Dimensions: $h/c = 2.25$, Re = 1,200,000

boundary layers and wakes can be continually refined until a specified spacing, *e.g.* a minimum value of y^+ for turbulent flows, is obtained. This procedure also removes the problem of having to guess *a priori* the location of the wakes. The adaption program starts with a mesh and a flow solution on that mesh. The average difference of the refinement flow variable between endpoints of all edges is computed. If the undivided difference of the flow variable across an edge is greater than a specified percent of this average, a node is added at the midpoint of the edge [12]. The new points are joined in so as to form quadrilaterals whenever possible and retain any structure of the original mesh. Mach number and entropy are typically used as the refinement variables. They allow for resolution of all relevant flow features: boundary layers, wakes, shocks, separation, and leading edge peaks. Figure 12 shows a sequence of meshes generated by this refinement process. The sequence of six meshes, not all of which are shown, reduced the spacing at the wall by a factor of 30. The flow solution is not reconverged on all intermediate meshes. Grid adaption would play an important role in the implementation of a multigrid algorithm.

3.3 Grids

The final grids for the four angles of attack investigated here are shown for $h/c = 2.25$ and Re = 1,200,000 in Figure 13. The dimensions of the grids are shown in Table 1. All the low Reynolds number grids have typical spacings at the airfoil of 6.E-05 chords ($y^+ < 10$) obtained by six levels of adaption. For the higher Reynolds number cases an extra level of adaption was required to achieve the desired wall spacing. The number

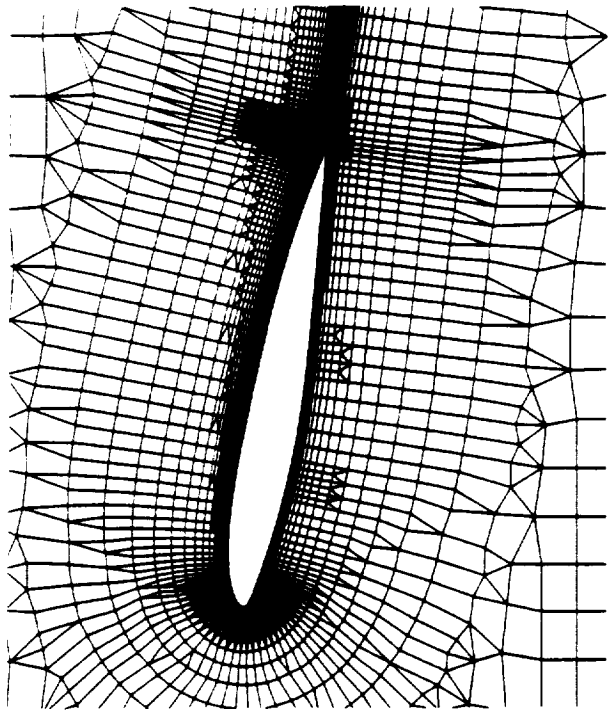

3)

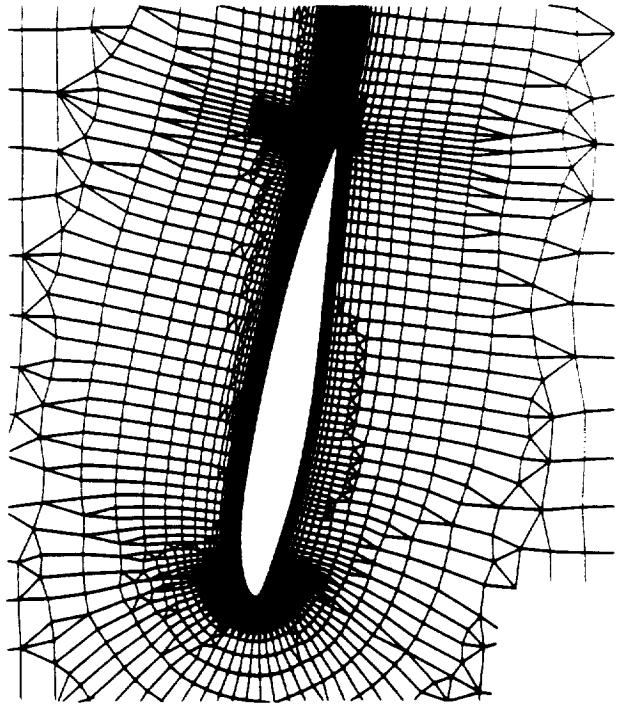

6)

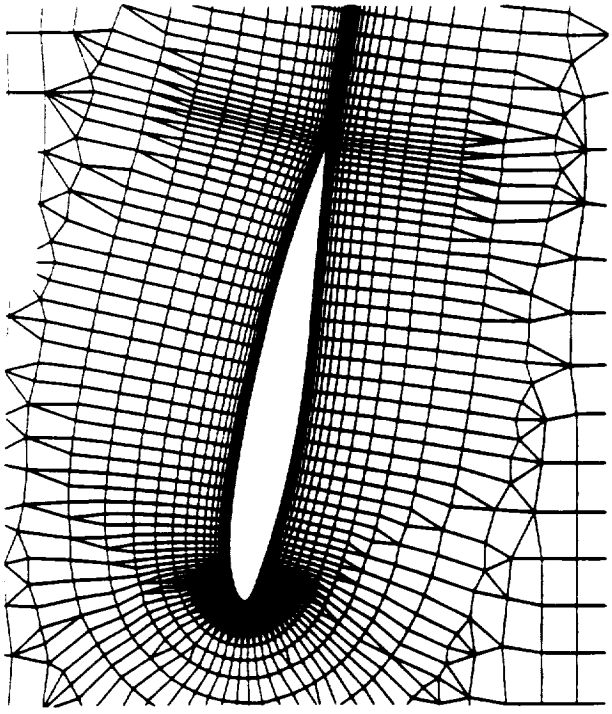

1)

Figure 12: Grid Adaption

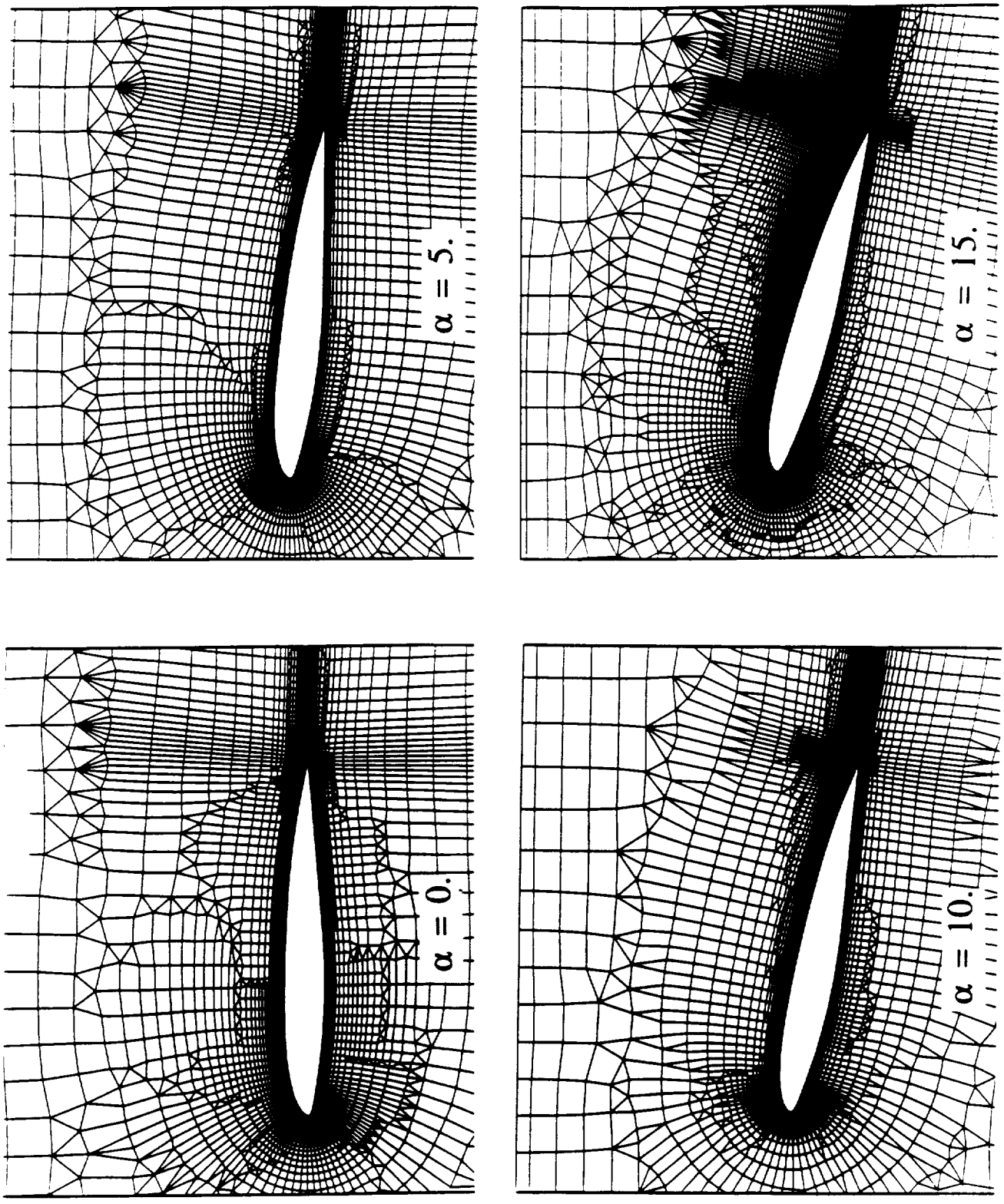

Figure 13: Grids for $h/c = 2.25$, $Re = 1{,}200{,}000$

of triangles is indicative of the amount of adaption as they are used to transition between levels of nested quadrilaterals. The smaller and larger height to chord ratios considered in this study subtract or add layers of quadrilateral cells to the wall. The meshes with height to chord ratio 4.5 add 1830 points (15 layers of quadrilateral cells) and $h/c = 1.5$ meshes subtract 488 points (5 layers of quadrilateral cells) from the $h/c = 2.25$ meshes. The background Cartesian wind tunnel grid has a constant spacing in the y direction of 0.075 chords and geometric stretching in the x direction. An example of the unconstrained grid is shown in Figure 14. It adds a C-mesh outer boundary and 1061 points to the $h/c = 4.5$ grid. Because the grids only change near the wind tunnel walls, grid effects can be ruled out as having any influence on the difference between solutions of varying h/c at a constant angle of attack. There are 61 points on each wall which extend from 5 chords upstream of the airfoil leading edge to 15 chords downstream.

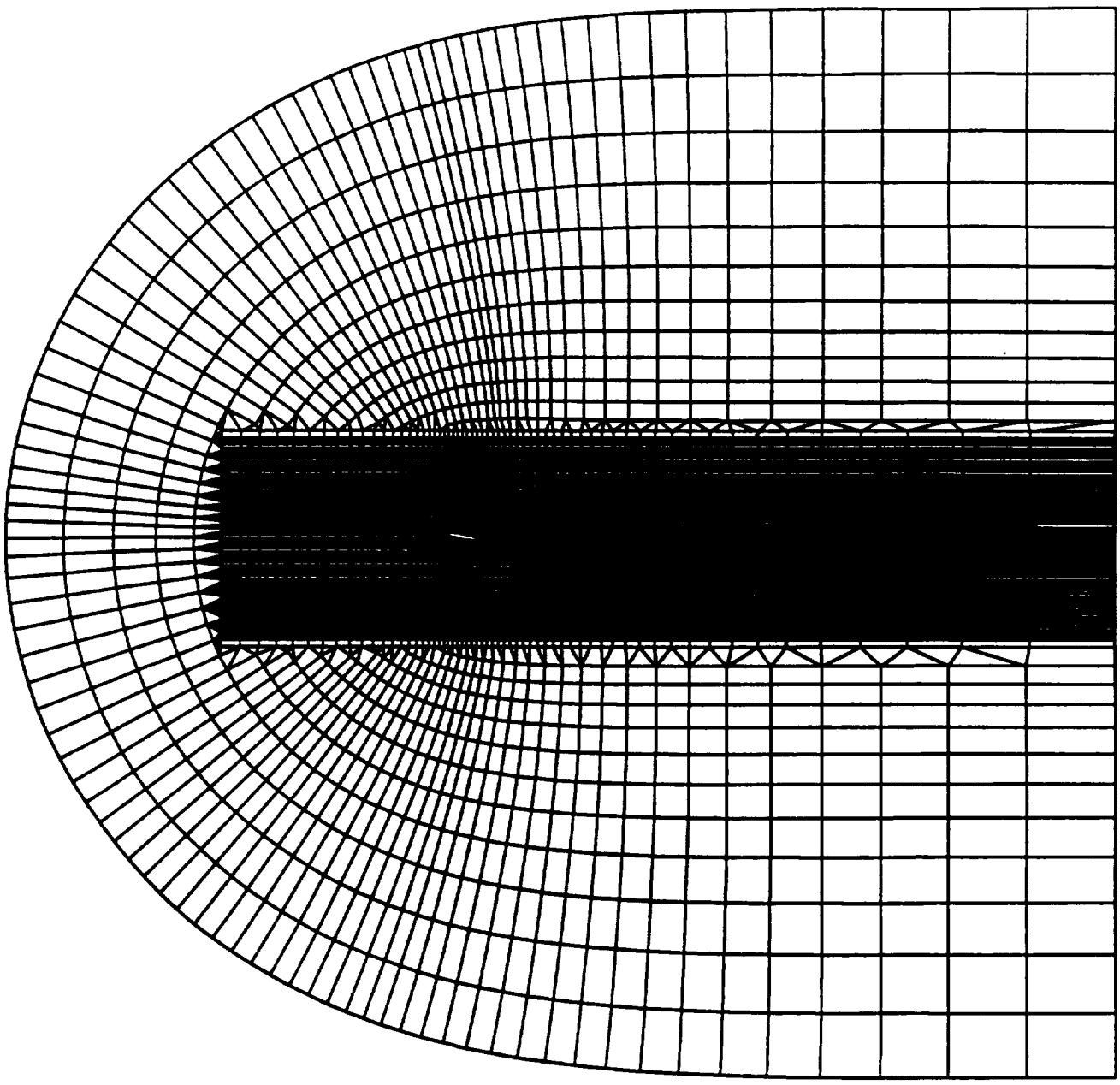

Figure 14: Grid for Unconstrained Flow

Chapter 4

Boundary Conditions

Boundary conditions are implemented in a manner consistent with the solution method in the interior of the domain. This usually involves a weak variational formulation of the boundary conditions. A control volume is constructed at the boundary points and fluxes through all segments are computed. For boundary control volumes this now includes a boundary flux (Figure 15). In this manner boundary conditions are only weakly enforced unless they are explicitly specified, for example, no slip: $u = v = 0$. Several boundary conditions are required for modeling wind tunnel flows.

4.1 Solid Walls

On the airfoil a no slip condition is applied. In addition the wall is specified as adiabatic and $\partial T/\partial n$ is set to zero in the boundary flux. The Navier-Stokes equations are integrated up to the wall using these specified variables. In this way continuity and normal momentum are automatically solved but with reduced accuracy at the wall due to the one-sided control volume. No extrapolations or approximate relations are used as in finite difference methods to enforce normal momentum and the adiabatic wall.

The wind tunnel walls are modeled as solid with a slip boundary condition. Although it would be a simple matter to include the wall boundary layer by increasing the grid point density near the walls so as to resolve them, in this study the effects of

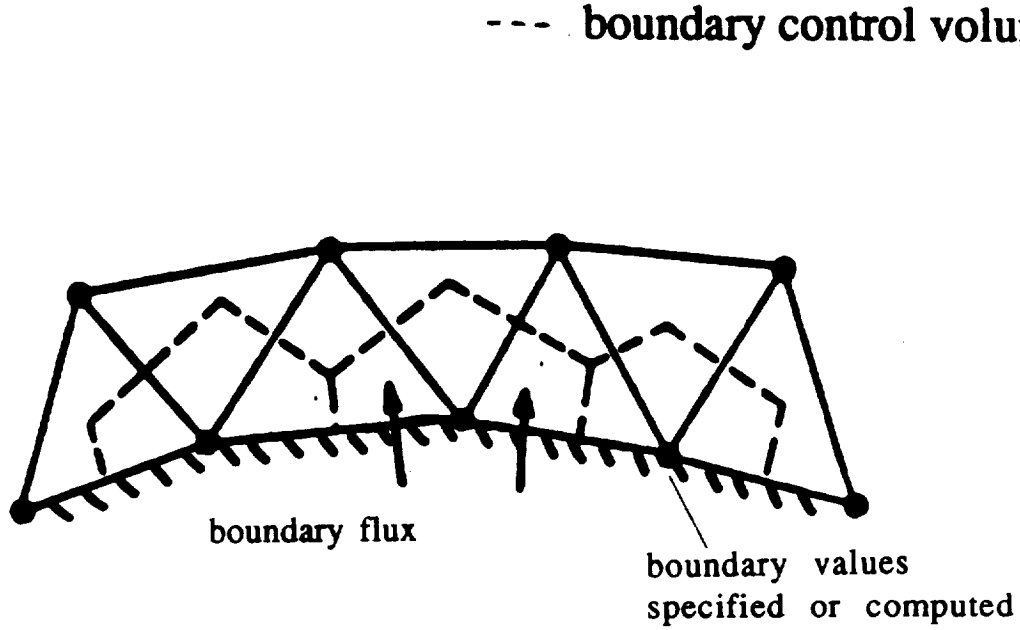

Figure 15: Weak Enforcement of Boundary Conditions

the wall boundary layers were not considered. Possible implications of a slip boundary condition are blowing and suction at the wall to remove the boundary layer or canting of the walls based on momentum thickness to negate boundary layer thickness effects. The wind tunnel walls are also adiabatic. The current implementation of a slip wall sets the normal velocity to zero at the end of each time step and sets the temperature gradient in the boundary flux. The tangential velocity component is extrapolated from the interior.

4.2 Inflow and Outflow

The information required for inflow or outflow is determined by the method of characteristics. For subsonic inflow there are three incoming characteristics which necessitate the specification of three quantities. The specified variables are the velocity tangential to the boundary, entropy, and the incoming Riemann invariant. The tangential velocity depends on the orientation of the boundary and is computed using $u = u_\infty$, $v = 0$. For the wind tunnel inflow plane, this is a parallel inflow assumption, $v_{tangential} = v = 0$, and is valid if the inflow plane is located far enough upstream. Entropy is set to its freestream value. The incoming Riemann invariant,

$$R_1 = u_{n_\infty} - \frac{2c_\infty}{\gamma - 1} \tag{17}$$

is the information carried on the one-dimensional, isentropic incoming characteristic [13], where u_{n_∞} is the velocity normal to the boundary at infinity. For the parallel inflow assumption, this equates to freestream. The outgoing Riemann invariant,

$$R_2 = u_{n_{extr}} - \frac{2c_{extr}}{\gamma - 1} \tag{18}$$

is extrapolated from the interior. The normal velocity and speed of sound at the boundary are then determined from

$$\begin{aligned} u_n &= \frac{1}{2}(R_1 + R_2) \\ c &= \frac{\gamma - 1}{2}(R_2 - R_1) \end{aligned} \tag{19}$$

The Cartesian velocities can be determined from the components of velocity normal and tangential to the boundary. Pressure and density are computed from the definition of the speed of sound $c^2 = \gamma p/\rho$ and the isentropic relation $s = p/\rho^\gamma$.

Exit boundary conditions for internal flow problems can be difficult to formulate unless outside information is available. For subsonic outflow one quantity must be specified due to the one incoming characteristic. Extrapolation of all quantities is unphysical and can prevent convergence or give poor results which depend on the initial conditions [14, 15]. Ideally, experimental wind tunnel pressures are desired. Since the calculations are not being directly compared to experimental results, there is no obvious quantity to specify at the outflow boundary. Therefore, the boundary was moved far downstream (15 chords) to minimize its influence on the rest of the flow field, and pressure was set to its freestream value. To damp out oscillations, a non-reflecting boundary condition based on the incoming characteristic is used [15]:

$$\frac{\partial p}{\partial t} - \rho c \frac{\partial u}{\partial t} + \alpha(p - p_\infty) = 0 \tag{20}$$

or numerically:

$$p_j^{n+1} = p_j^n + \rho^n c^n \Delta t(u_j^{n+1} - u_j^n) - \alpha \Delta t(p_j^n - p_\infty) \tag{21}$$

This helps but does not eliminate reflection of pressure disturbances back into the wind tunnel where they bounce between the exit and entrance plane and the walls. At steady state ($\partial/\partial t = 0$) the outflow pressure reaches p_∞. The remaining variables are extrapolated. The inflow and outflow boundary conditions used for the wind tunnel case can also be used in the unconstrained case. For the C-mesh used on the outer boundary, the orientation of the inflow boundary now determines the tangential and normal directions which are not always aligned with the Cartesian directions.

Chapter 5

Discussion

Four angles of attack (α = 0, 5, 10, and 15 degrees), three total wind tunnel height to airfoil chord ratios (h/c = 1.5, 2.25, and 4.5), and two Reynolds numbers (Re = 1,200,000 and 6,000,000) were computed. The intermediate height to chord ratio of 2.25 was not run for the higher Reynolds number. The unconstrained case was simulated using an outer boundary diameter of 24 chords and appropriate boundary conditions. All cases use a freestream Mach number of 0.25. In this chapter, the results from the CFD runs will be presented and discussed.

5.1 Results

At zero degrees angle of attack, the airfoil is generating a small amount of lift. Figure 16 shows negative pressure coefficients on the airfoil for h/c = 1.5, 2.25, and the unconstrained case at the lower Reynolds number while Figure 17 compares distributions at the two Reynolds numbers. The pressure distributions vary only slightly. The stagnation point at zero degrees angle of attack is right at the leading edge and bumps and flat spots in the geometry are indicated by the bumps and spikes in the solution on both the pressure and suction sides of the airfoil. The pressure side leading edge spike is seen to go away as the stagnation point moves back at higher angles of attack. Plots of skin friction coefficient, C_f, are shown in Figures 18 and 19 for the low and high Reynolds numbers respectively. Trends are similar, but the low

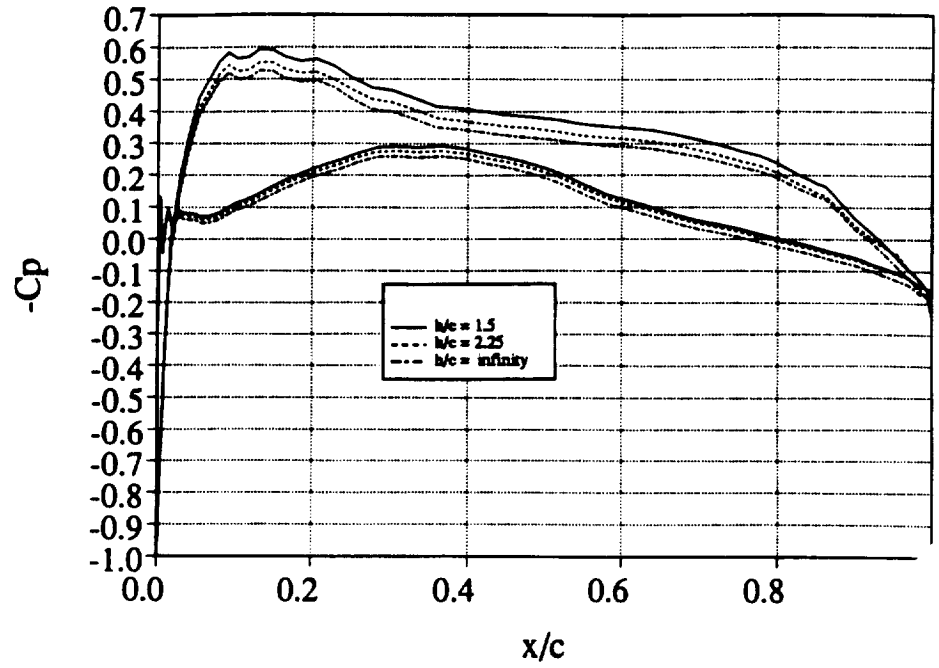

Figure 16: Airfoil Pressures: $\alpha = 0$ degrees, Re = 1,200,000

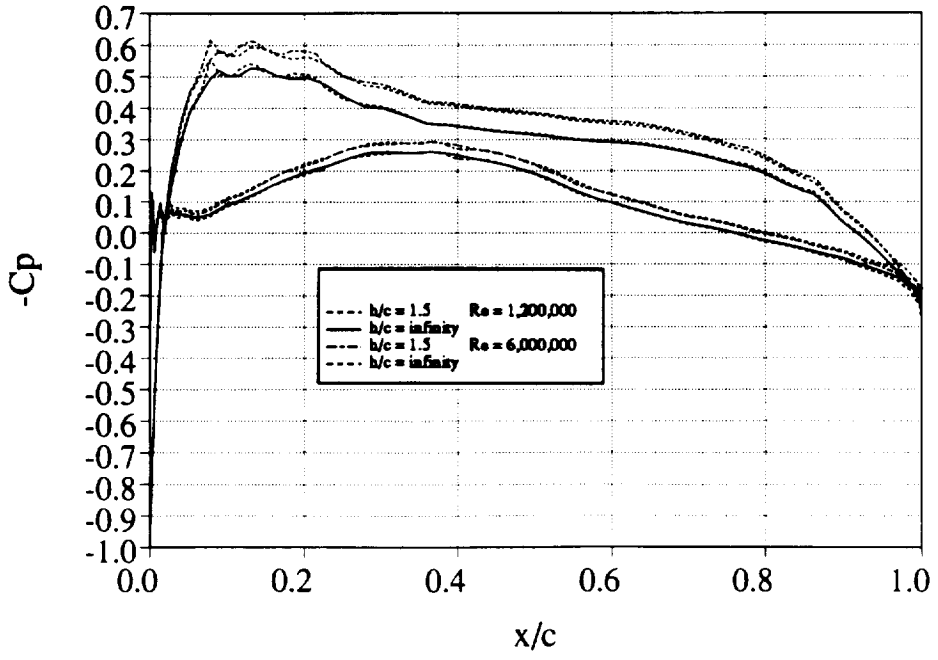

Figure 17: Airfoil Pressures: $\alpha = 0$ degrees

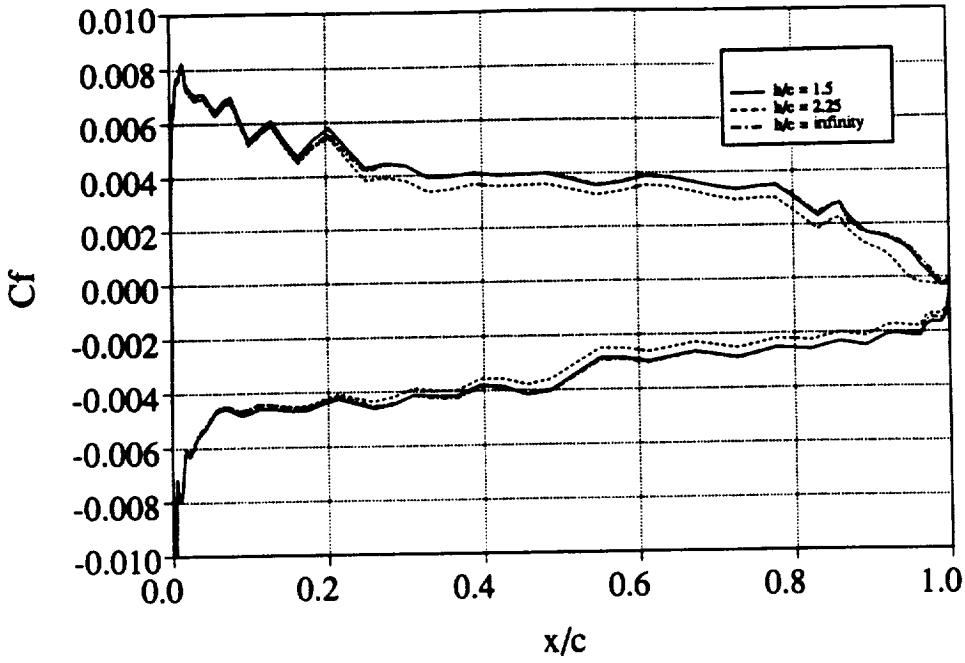

Figure 18: Airfoil Skin Friction: $\alpha = 0$ degrees, $Re = 1{,}200{,}000$

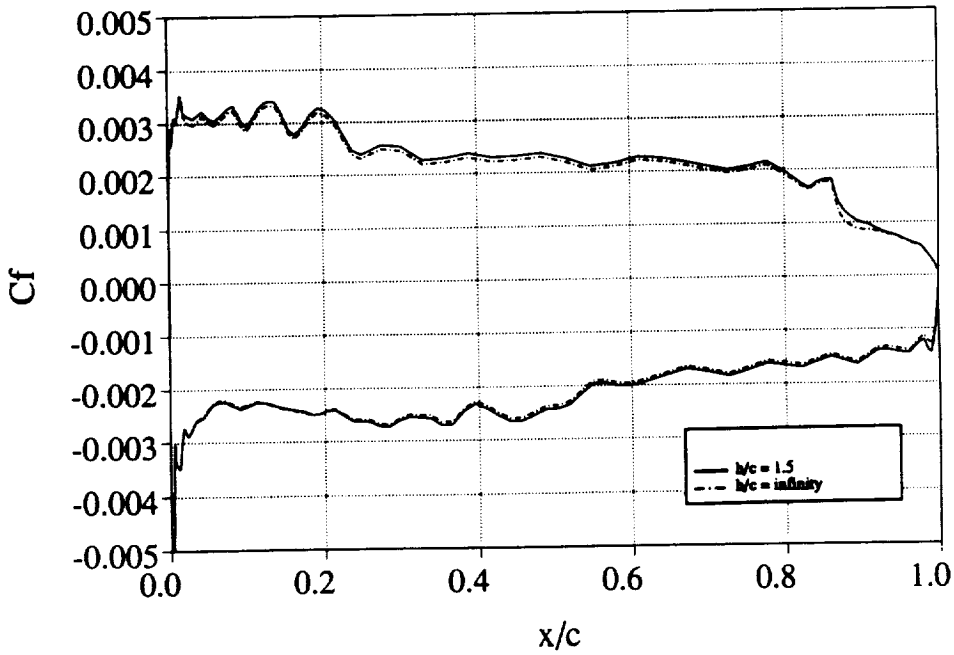

Figure 19: Airfoil Skin Friction: $\alpha = 0$ degrees, $Re = 6{,}000{,}000$

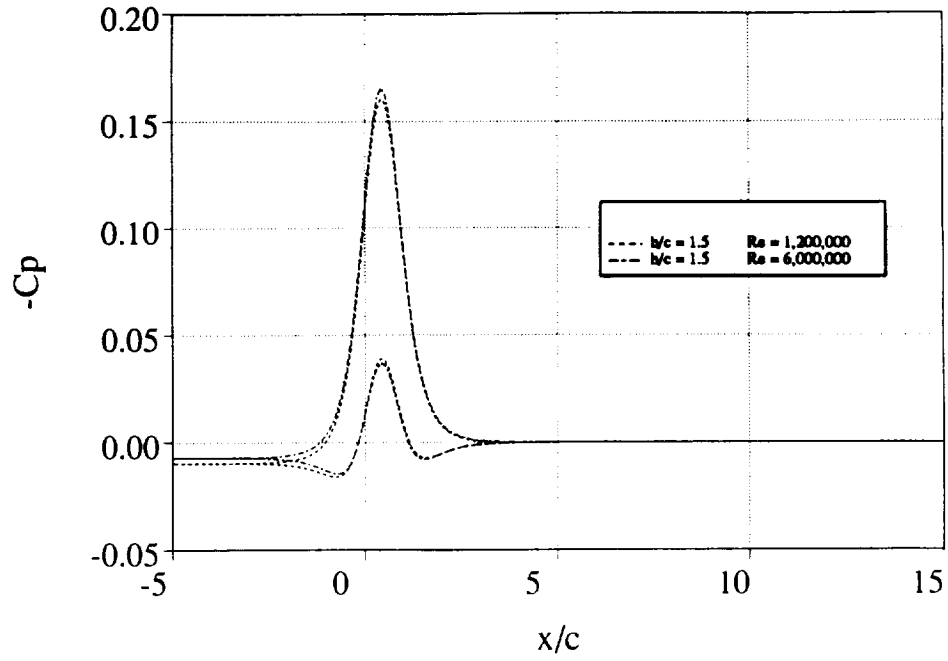

Figure 20: Wall Pressures: $\alpha = 0$ degrees

Reynolds number case shows a small amount of trailing edge separation and increased C_f. Portions of the upper and lower surfaces would be laminar if a transition model were implemented, *i.e.* if the flow were not tripped at the leading edge. Figure 20 is a plot of wall pressures for the confined flow cases. The effects here can be considered as the addition of a potential source and vortex. The source represents blockage. The vortex adds the small amount of lift. Effects from a source would be symmetric about the centerline on the top and bottom walls, while the vortex would show an antisymmetric distribution. Both are seen to influence the wall distribution. Because of the Riemann invariant boundary conditions at the inflow, the incoming Mach number and pressure will not necessarily be freestream values, but the exit pressure decays to the prescribed freestream value.

Similar plots of airfoil pressure distributions, skin friction coefficients, and wall pressure distributions for the five degrees angle of attack case are shown in Figures 21 through 25. As expected the lift increases as the walls are moved in (Figure 21), but Reynolds number is seen to have very little effect on the airfoil pressure distributions

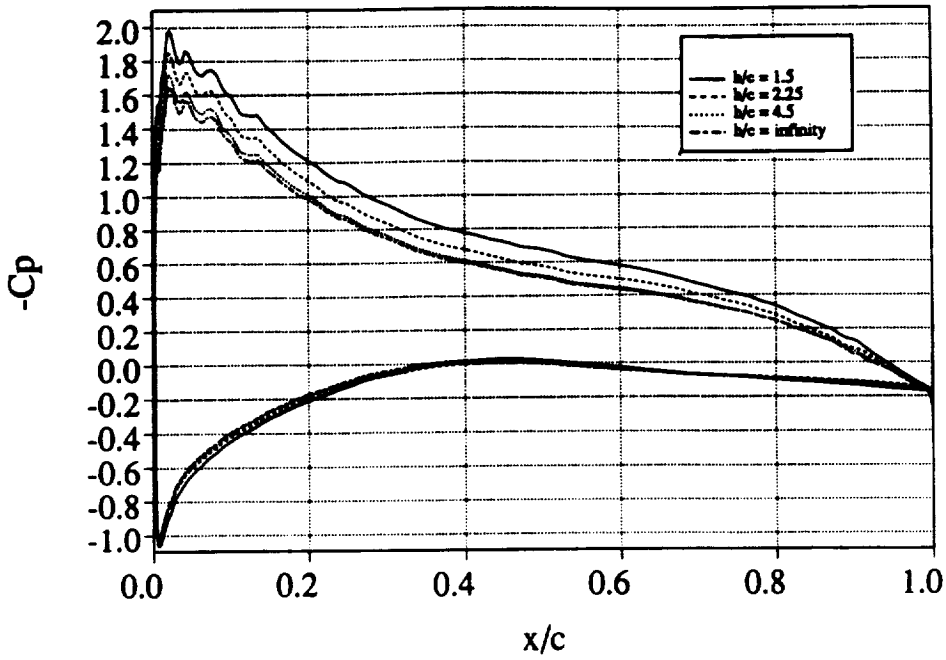

Figure 21: Airfoil Pressures: $\alpha = 5$ degrees, $Re = 1{,}200{,}000$

(Figure 22). The skin friction plots for the two Reynolds numbers, Figures 23 and 24, indicate no effect of wall proximity on the small recirculation region present at the trailing edge except for the unconstrained, low Reynolds number case where this region is slightly reduced. The recirculation region begins at the separation point where C_f equals zero and extends to the trailing edge. The region is indicated by the negative, almost zero skin friction coefficient and is smaller at the higher Reynolds number. The major effect seen in the wall pressures is that of a vortex (Figure 25). Reynolds number has no influence at the slip walls. Typical flowfields are shown in the Mach number contour plots of Figures 26 and 27 at five degrees angle of attack for the the height to chord ratio of 1.5 and the unconstrained runs. Basic qualitative features of the wind tunnel flows are illustrated, for example, reduced wake curvature and the confining effects of the walls.

Figure 28 shows the effect of wall proximity for the ten degrees angle of attack case and $Re = 1{,}200{,}000$. Effects of higher Reynolds number are shown in Figure 29 where some differences are apparent for the constrained cases, especially the lowest height

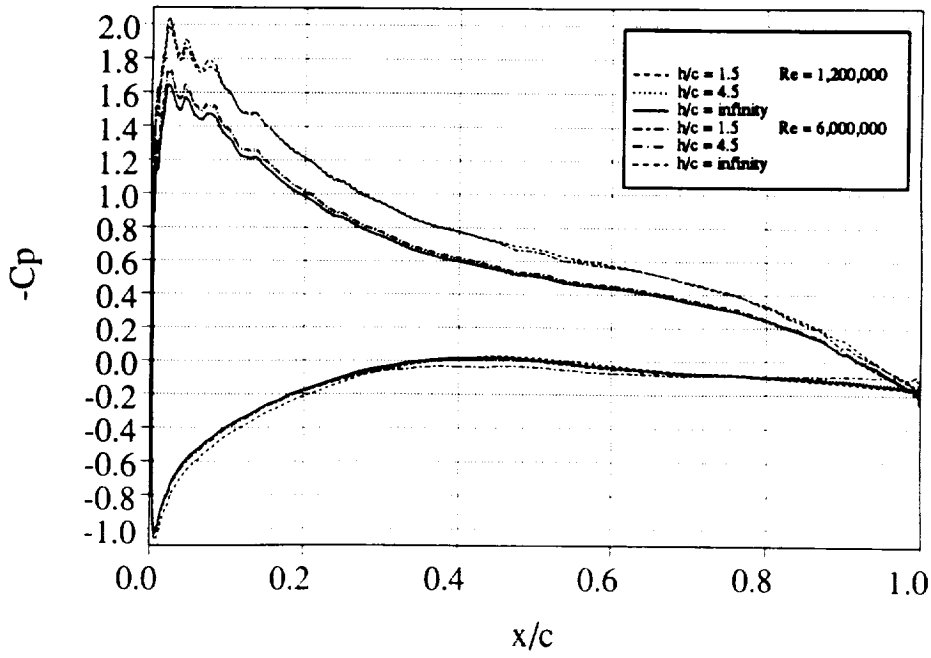

Figure 22: Airfoil Pressures: $\alpha = 5$ degrees

to chord ratio. The grid adaption allows the leading edge peak to be accurately captured. Figures 30 and 31 show skin friction plot for Reynolds numbers of 1.2 and 6.0 million, respectively. They indicate a reduced recirculation region at the trailing edge as h/c is increased. This is due to the decreased levels of lift which delay separation. Wall pressures are shown in Figure 32 where the Reynolds number effects at the airfoil are reflected.

Results for the fifteen degrees angle of attack case are presented in Figures 33 through 38. Figures 33 and 34 are airfoil C_p distributions. The critical pressure coefficient, C_p^*, at $M = 1.0$ is -10.2, so that for this configuration the flow becomes supersonic over the leading edge. Figure 35, a Mach number contour plot of the leading edge of the airfoil for the high Reynolds number, small height to chord ratio case, shows a small shock which appears at this angle of attack. This is probably caused in part by the irregular geometry in this region. The boundary layer thickens considerably behind the shock. For $h/c = 1.5$ and $Re = 6{,}000{,}000$ the peak Mach number is 1.70. For $Re = 1{,}200{,}000$ the peak Mach number is 1.62, while for the

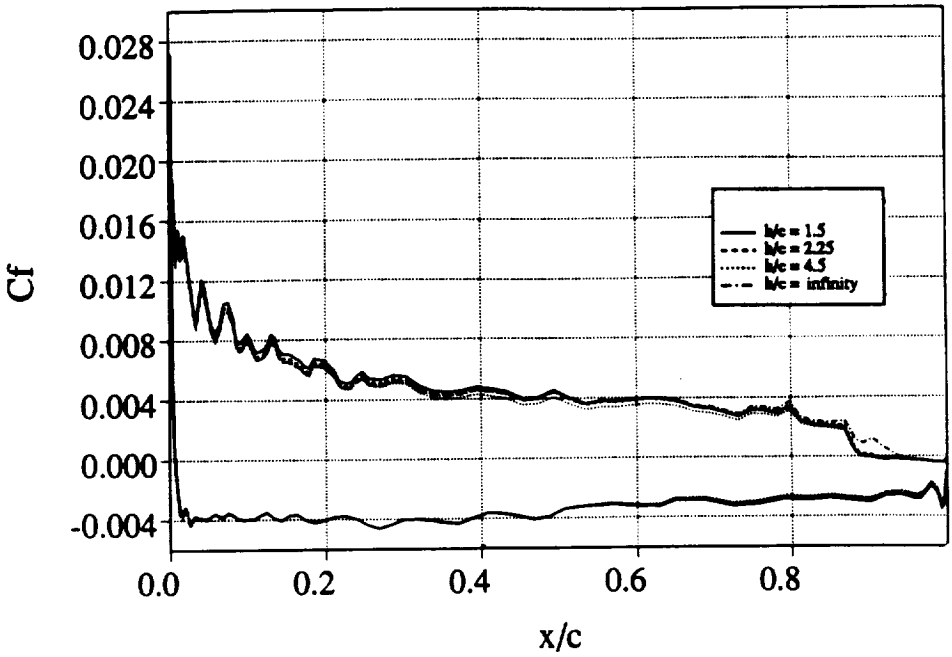

Figure 23: Airfoil Skin Friction: $\alpha = 5$ degrees, Re = 1,200,000

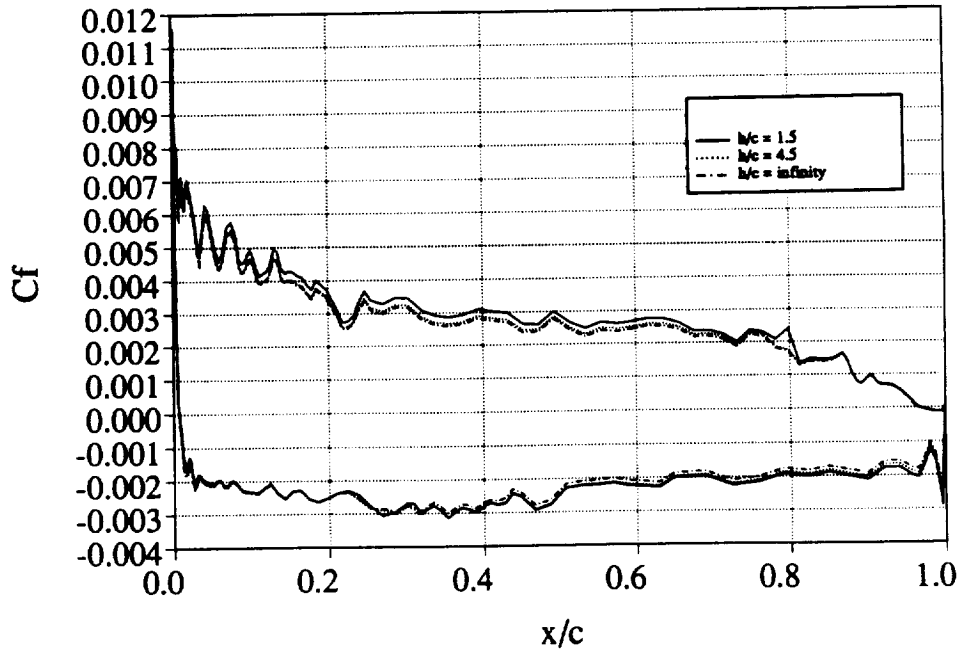

Figure 24: Airfoil Skin Friction: $\alpha = 5$ degrees, Re = 6,000,000

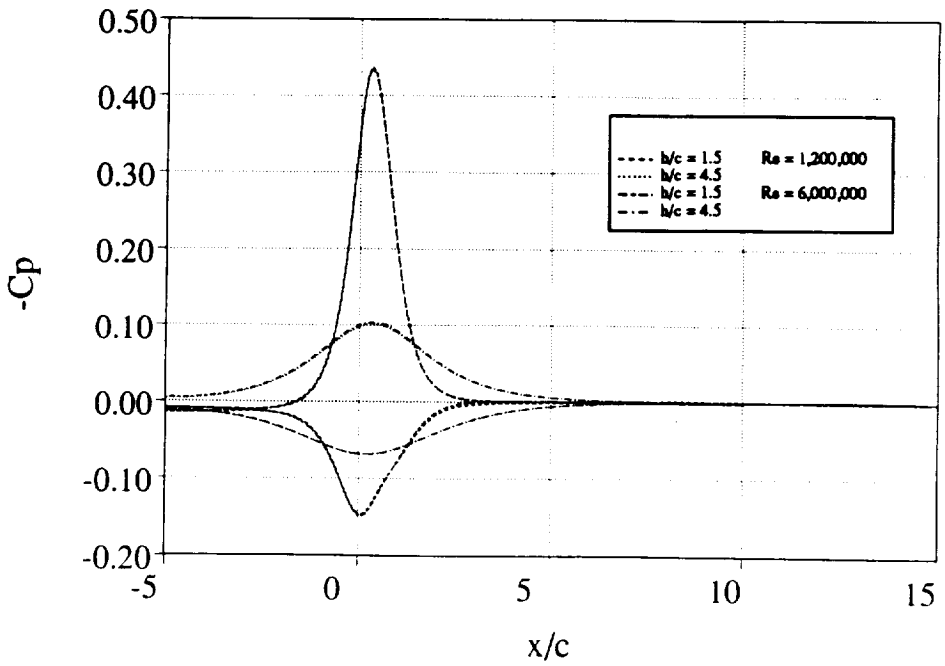

Figure 25: Wall Pressures: $\alpha = 5$ degrees

unconstrained case at this Reynolds number it is 1.45. The skin friction plot for the lower Reynolds number (Figure 36) indicates leading edge separation, reattachment, and separation again over much of the rear of the airfoil with the extent of the separation dependent on height to chord ratio. For the higher Reynolds number the leading edge separation is reduced (Figure 37). Wall pressures are shown in Figure 38 for both Reynolds numbers. Despite the differences in the behavior of the skin friction, Reynolds number has relatively little effect on the airfoil and wall pressure distributions. The wake curvature is more apparent in the Mach number contour plots of Figures 39 and 40 with the airfoil at fifteen degrees angle of attack. Here the larger separation region and thicker boundary layer and wake of the lowest height to chord ratio configuration are compared with the unconstrained solution.

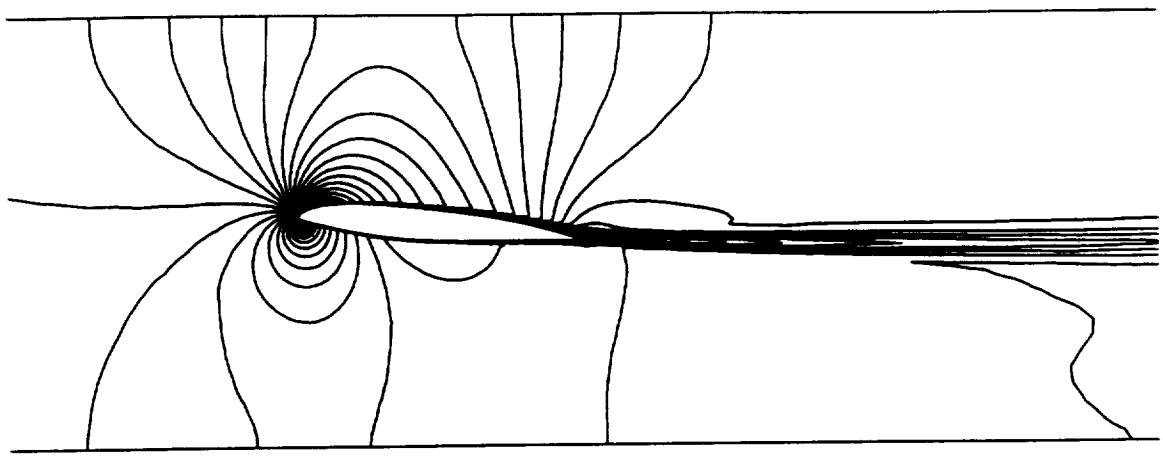

Figure 26: Mach Number Contours: $\alpha = 5$ degrees, $h/c = 1.5$, Re = 1,200,000

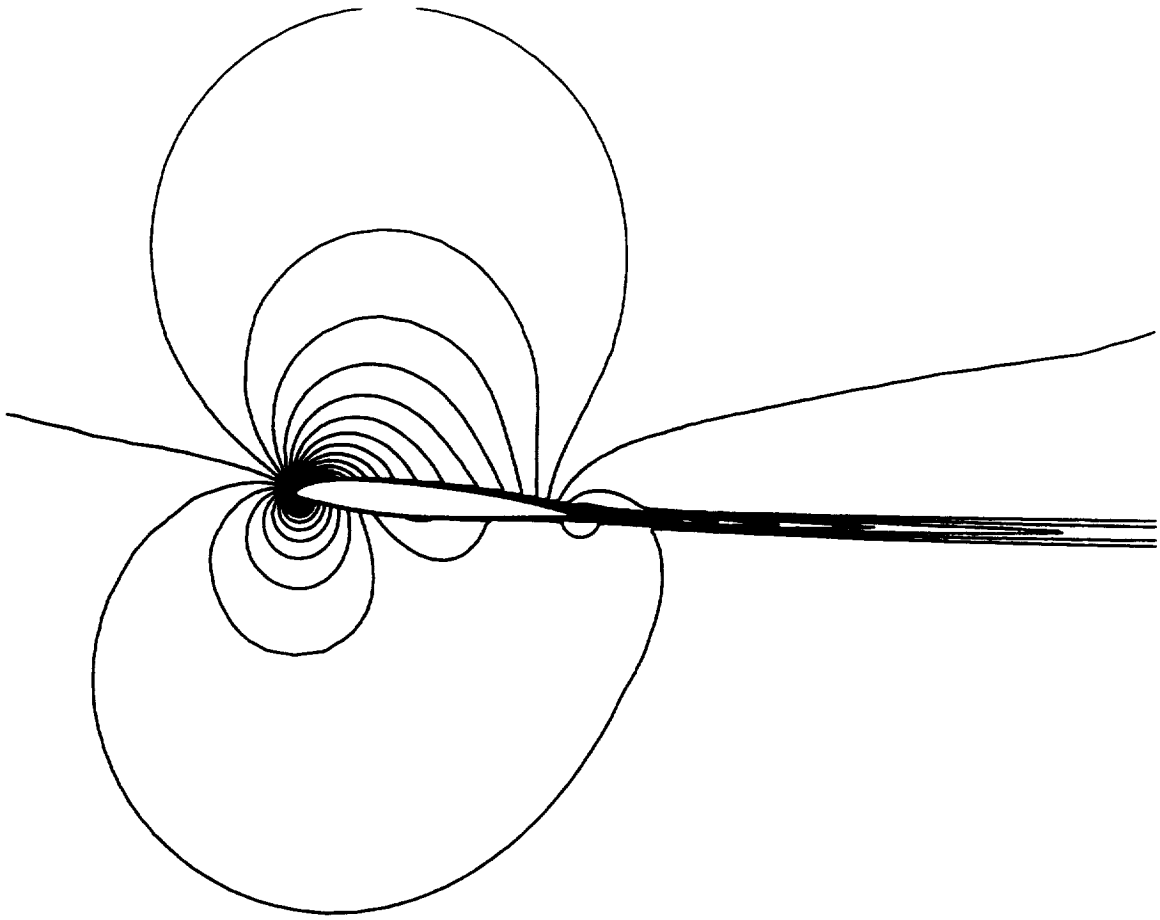

Figure 27: Mach Number Contours: $\alpha = 5$ degrees, unconstrained, Re = 1,200,000

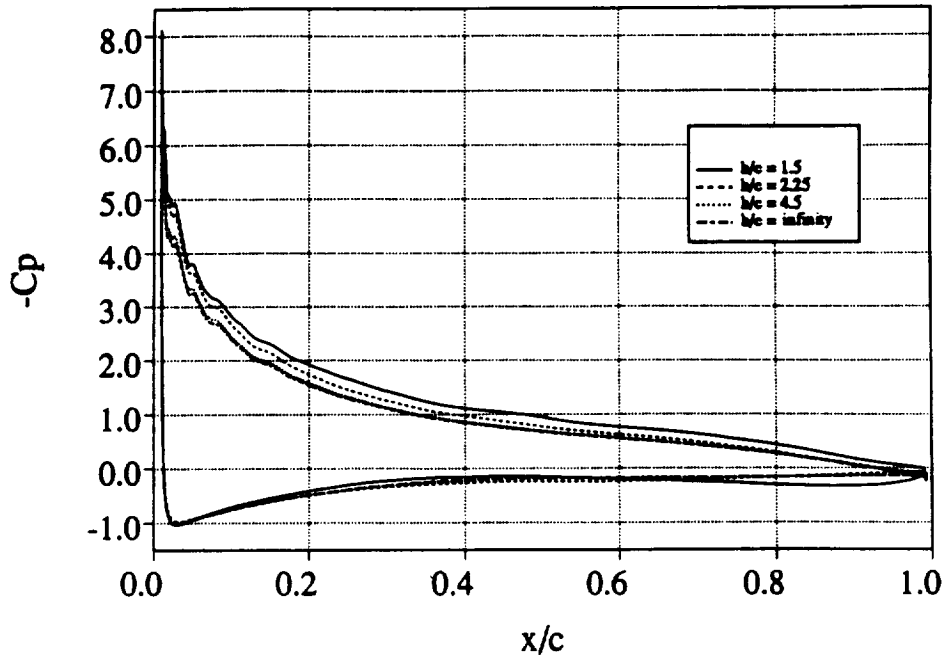

Figure 28: Airfoil Pressures: $\alpha = 10$ degrees, $Re = 1{,}200{,}000$

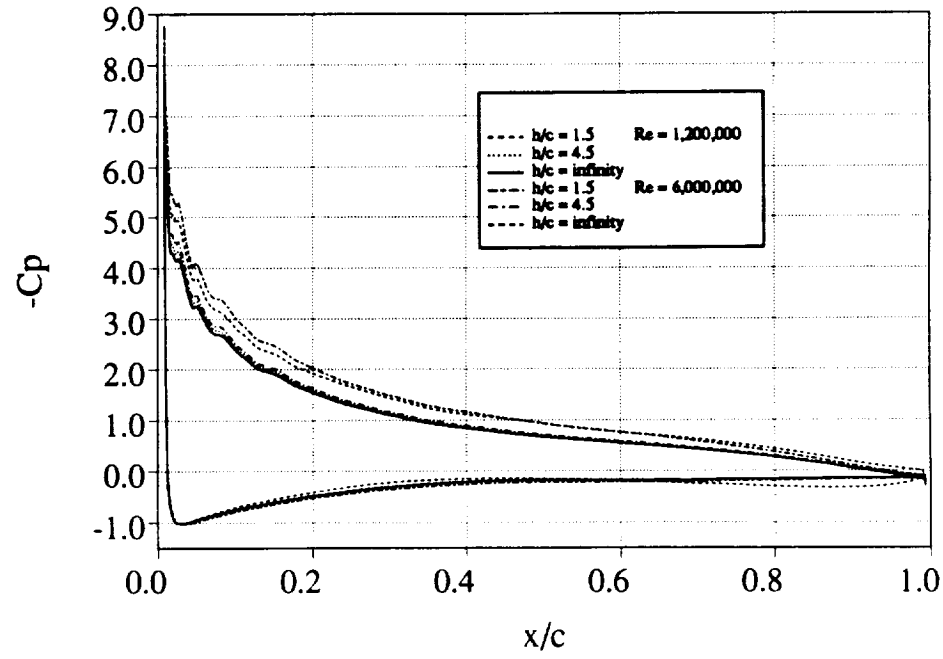

Figure 29: Airfoil Pressures: $\alpha = 10$ degrees

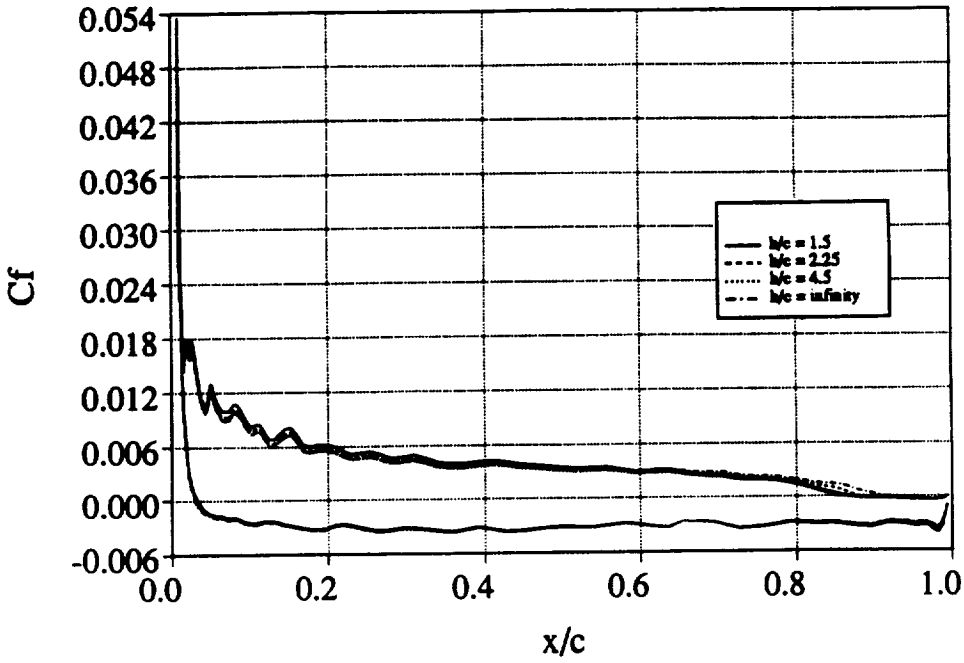

Figure 30: Airfoil Skin Friction: $\alpha = 10$ degrees, $Re = 1{,}200{,}000$

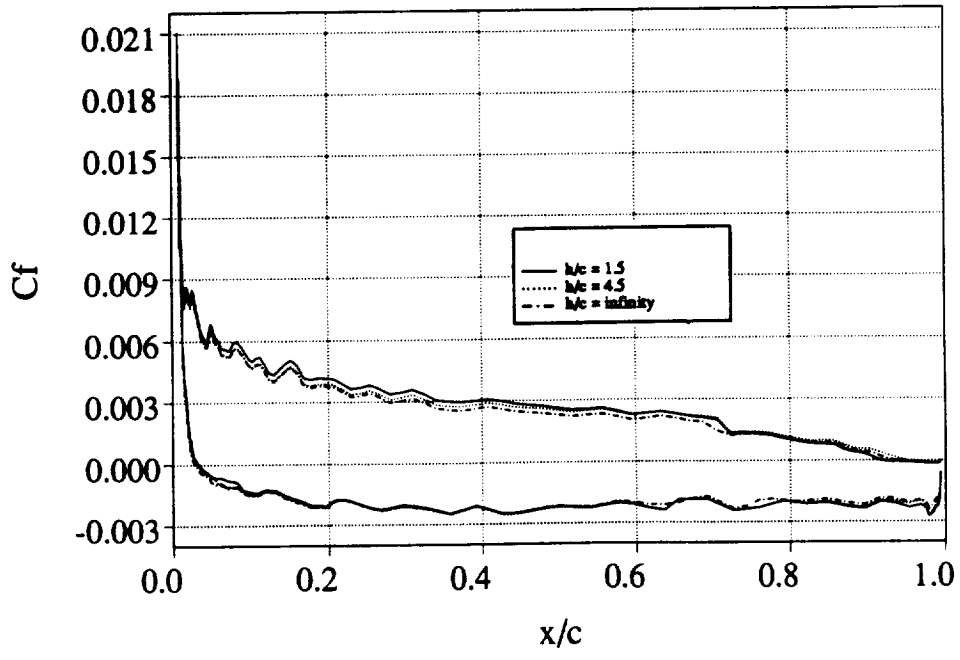

Figure 31: Airfoil Skin Friction: $\alpha = 10$ degrees, $Re = 6{,}000{,}000$

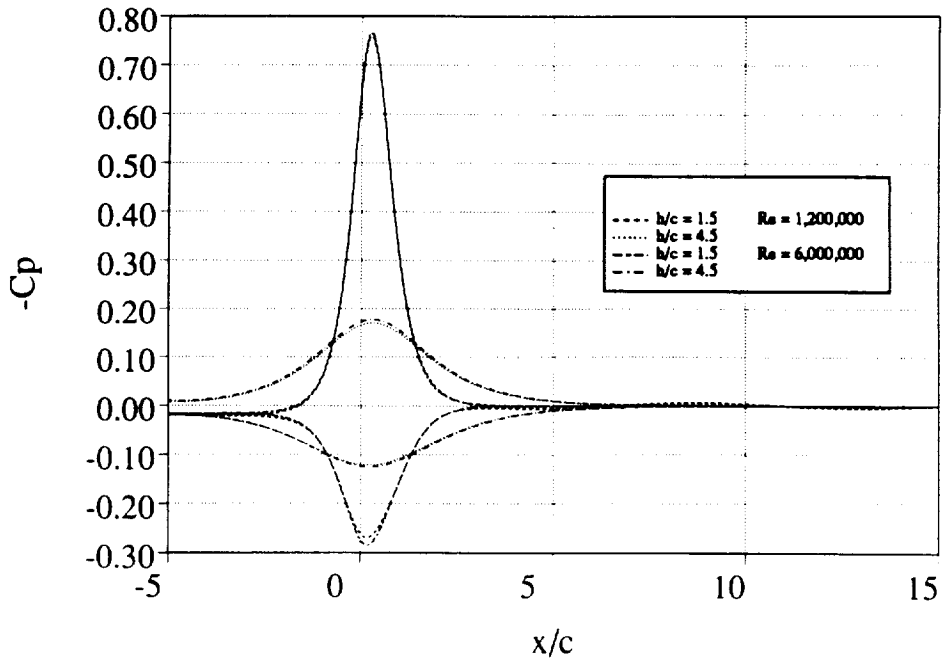

Figure 32: Wall Pressures: $\alpha = 10$ degrees

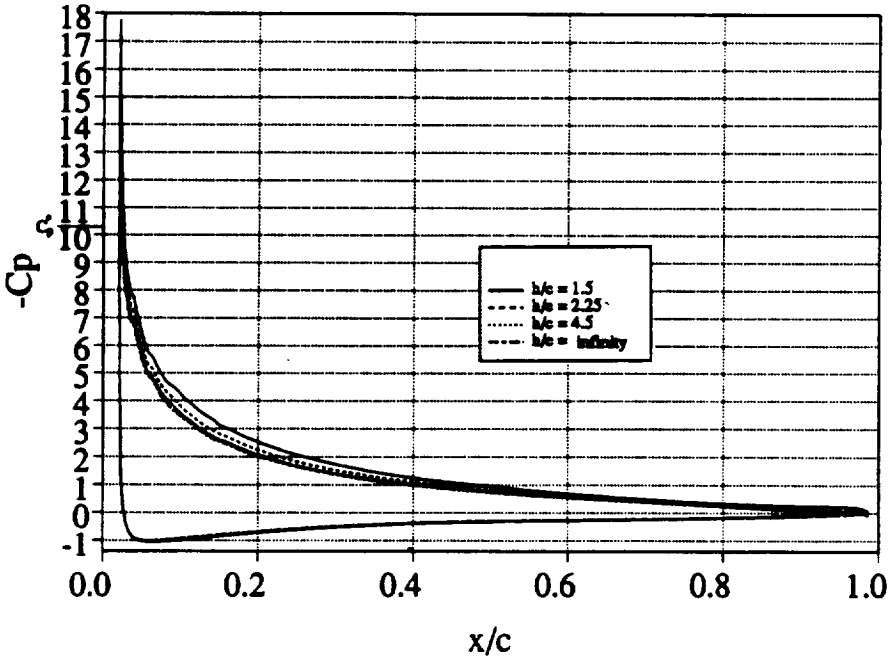

Figure 33: Airfoil Pressures: $\alpha = 15$ degrees, $Re = 1{,}200{,}000$

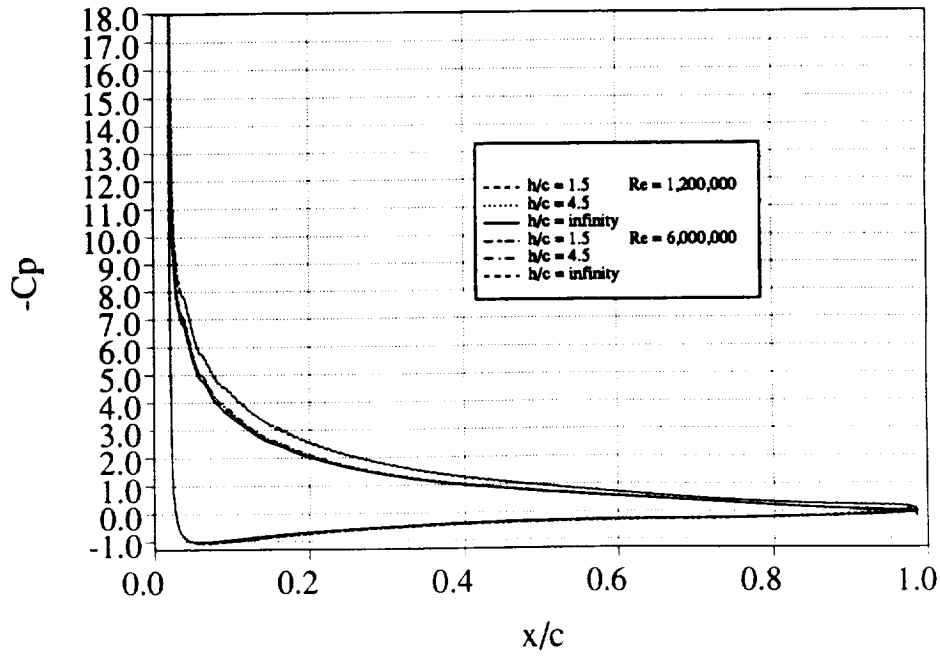

Figure 34: Airfoil Pressures: $\alpha = 15$ degrees

5.2 Lift

Table 2 summarizes the lift and drag coefficients as a function of wind tunnel height, Reynolds number, and angle of attack. Trends in the lift coefficient show that in all cases it increases with decreasing wind tunnel wall height to chord ratio. This is due to the wall induced upwash [16] and the vortex reflection and acceleration effects the walls have on the flow. Increasing the Reynolds number tended to increase the lift coefficient slightly, by at most 6%, with the largest percentage changes occurring at small h/c. The small variations of pressure coefficient with Reynolds number are seen in Figures 17, 22, 29, and 34. It seems that increasing the Reynolds number has, to a much lesser extent, the same effect on lift as decreasing the height to chord ratio.

Figure 41 shows lift coefficient versus angle of attack for the four height to chord ratios. Up to ten degrees where the flow is almost fully attached, the data indicates the effect of decreasing h/c or increasing Reynolds number is to linearly displace the lift curve upward and increase its slope. Even in the region near stall past ten degrees angle of attack where the lift curves level off and viscous phenomenon play

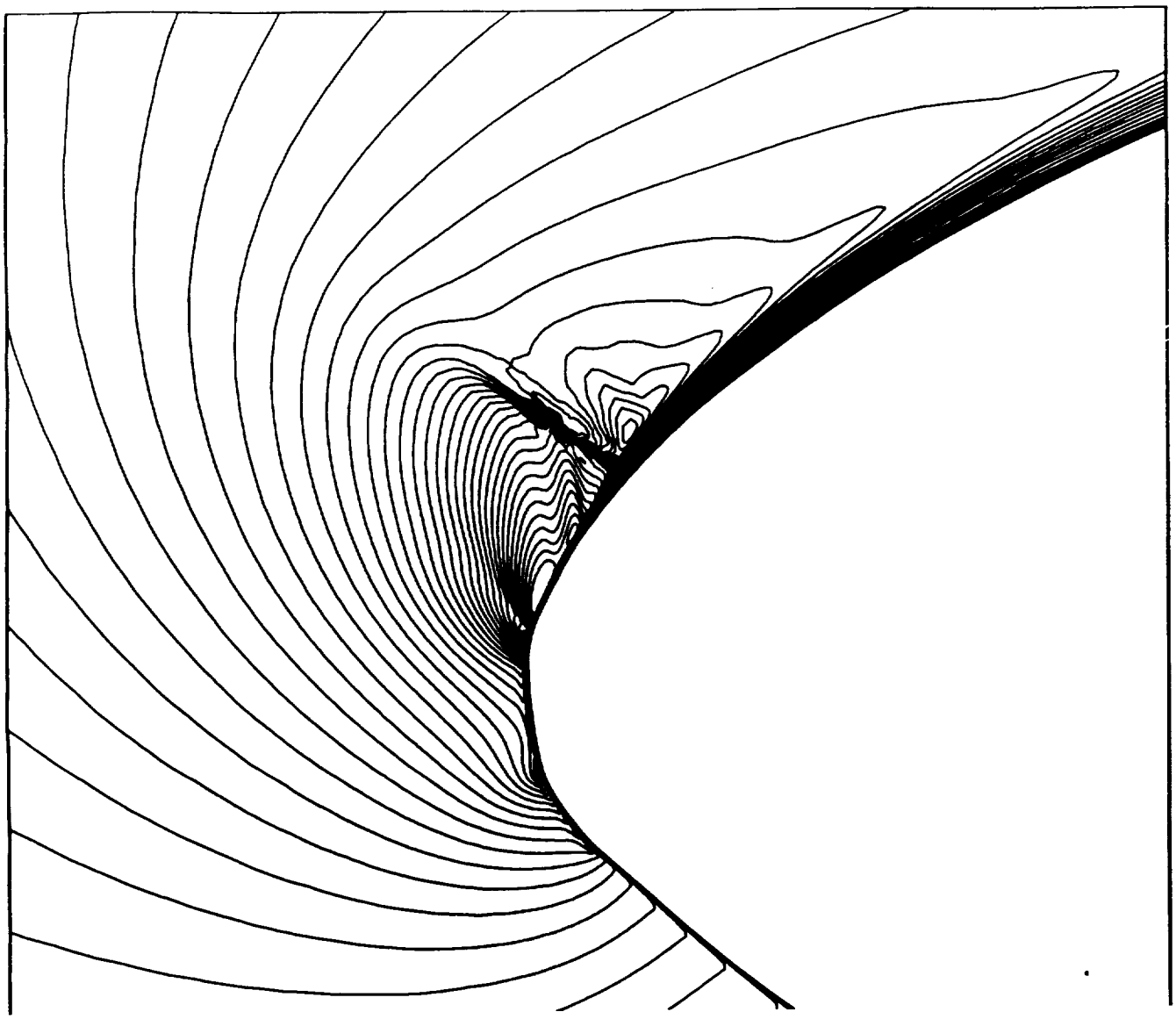

Figure 35: Blow Up of Leading Edge Mach Number Contours: $\alpha = 15$ degrees, $h/c = 1.5$, $Re = 6{,}000{,}000$

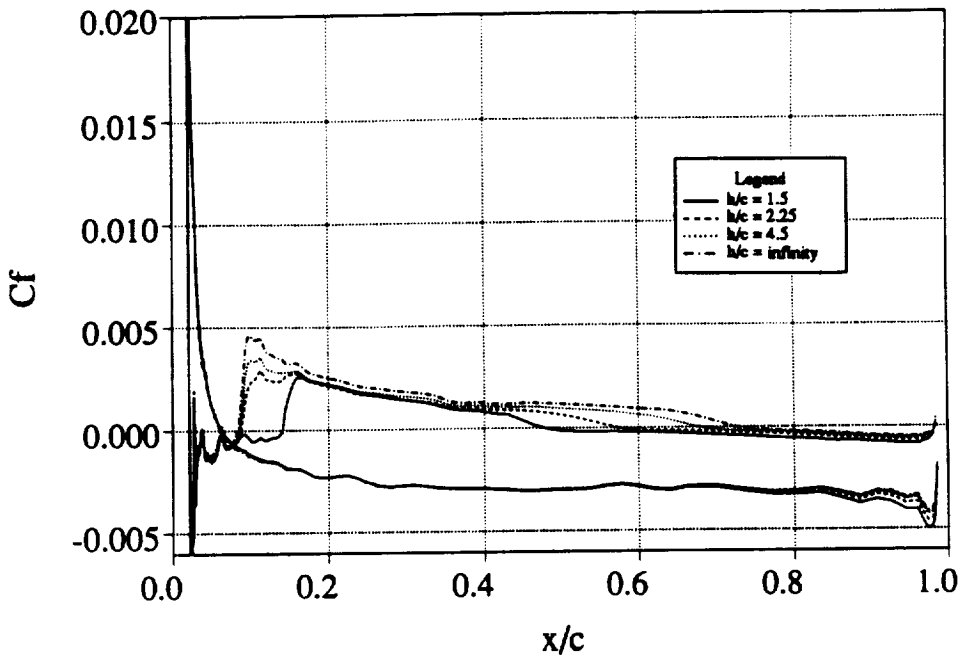

Figure 36: Airfoil Skin Friction: $\alpha = 15$ degrees, $Re = 1{,}200{,}000$

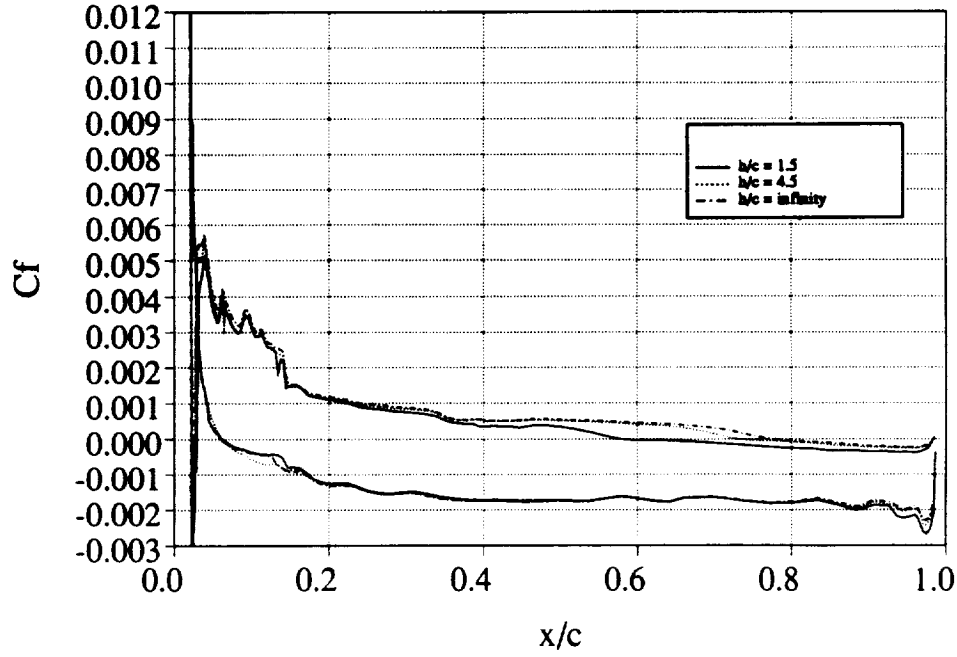

Figure 37: Airfoil Skin Friction: $\alpha = 15$ degrees, $Re = 6{,}000{,}000$

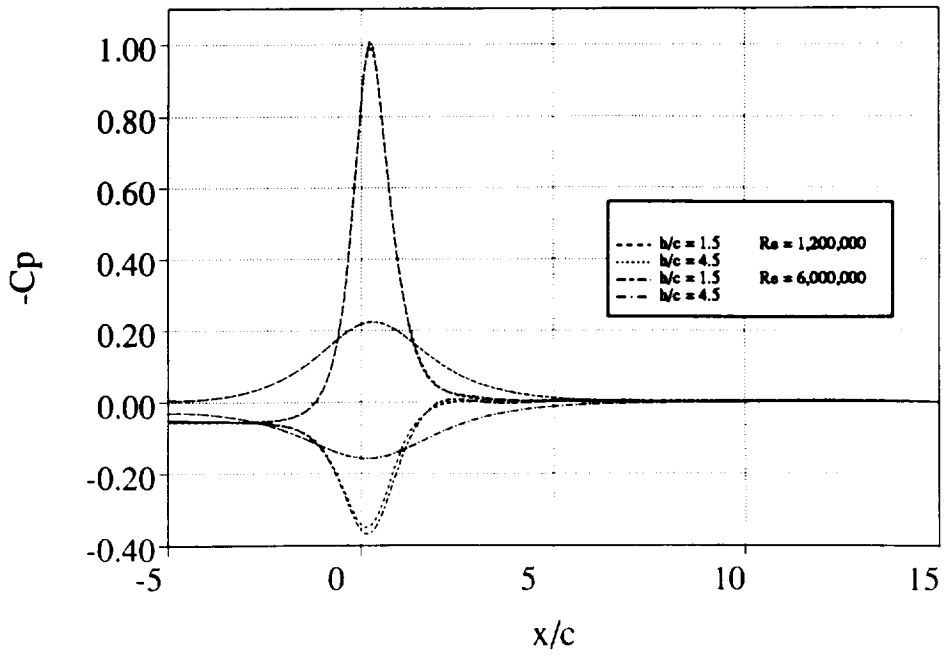

Figure 38: Wall Pressures: $\alpha = 15$ degrees

α (degrees)		0		5		10		15	
h/c	Re	C_l	C_d	C_l	C_d	C_l	C_d	C_l	C_d
1.5	1,200,000	.2059	.0105	.8989	.0168	1.5393	.0320*	1.9084	.0755
1.5	6,000,000	.2195	.0067	.8933	.0076*	1.5889	.0179	1.9599	.0736
2.25	1,200,000	.1843	.0101	.8085	.0127	1.3904	.0153*	1.7407	.0576
4.5	1,200,000	–	–	.7442	.0121	1.2788	.0195	1.6463	.0483
4.5	6,000,000	–	–	.7561	.0091	1.3223	.0143	1.6594	.0403
∞	1,200,000	.1777	.0100	.7240	.0142	1.2465	.0225	1.5802	.0476
∞	6,000,000	.1861	.0064	.7204	.0106	1.2427	.0191	1.6019	.0442

* significant error

Table 2: Lift and Drag Coefficients

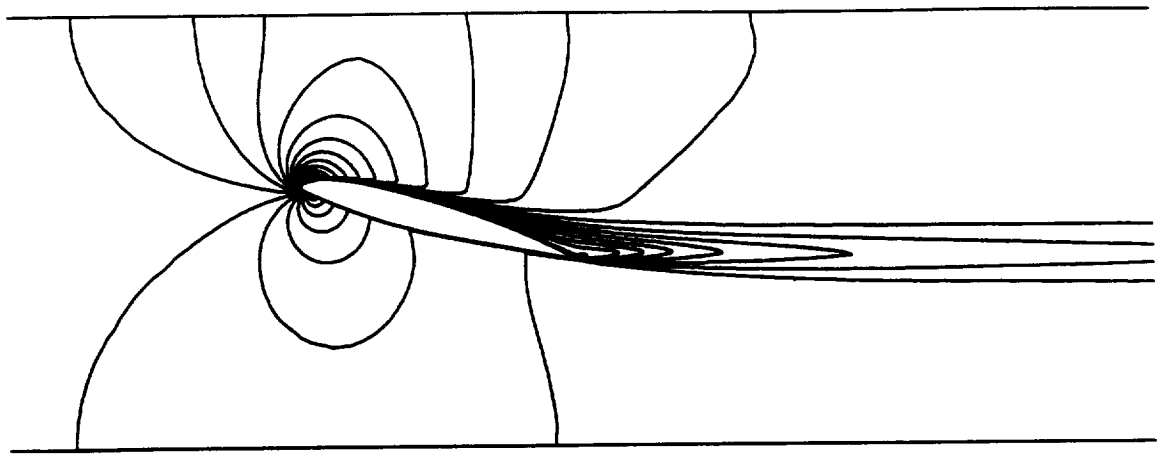

Figure 39: Mach Number Contours: $\alpha = 15$ degrees, $h/c = 1.5$, $Re = 1{,}200{,}000$

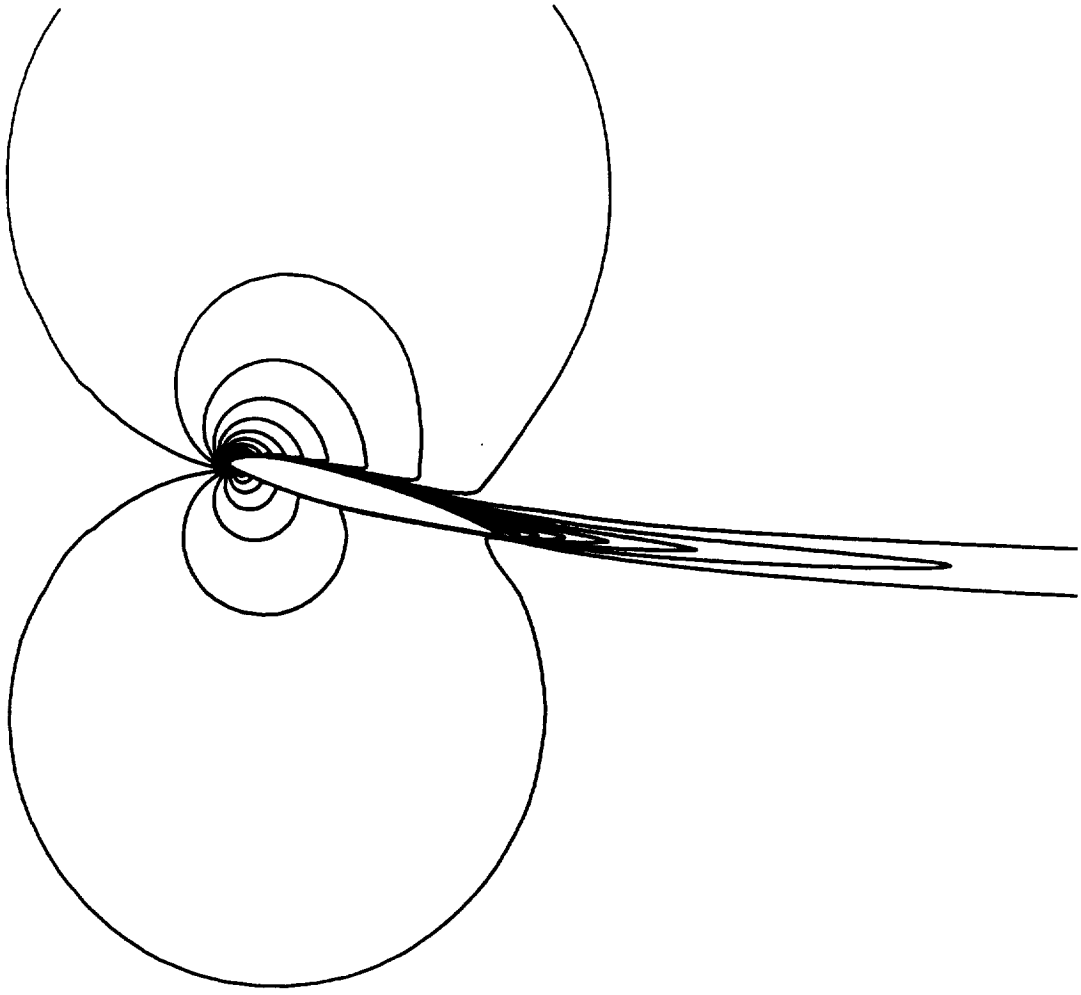

Figure 40: Mach Number Contours: $\alpha = 15$ degrees, unconstrained, $Re = 1{,}200{,}000$

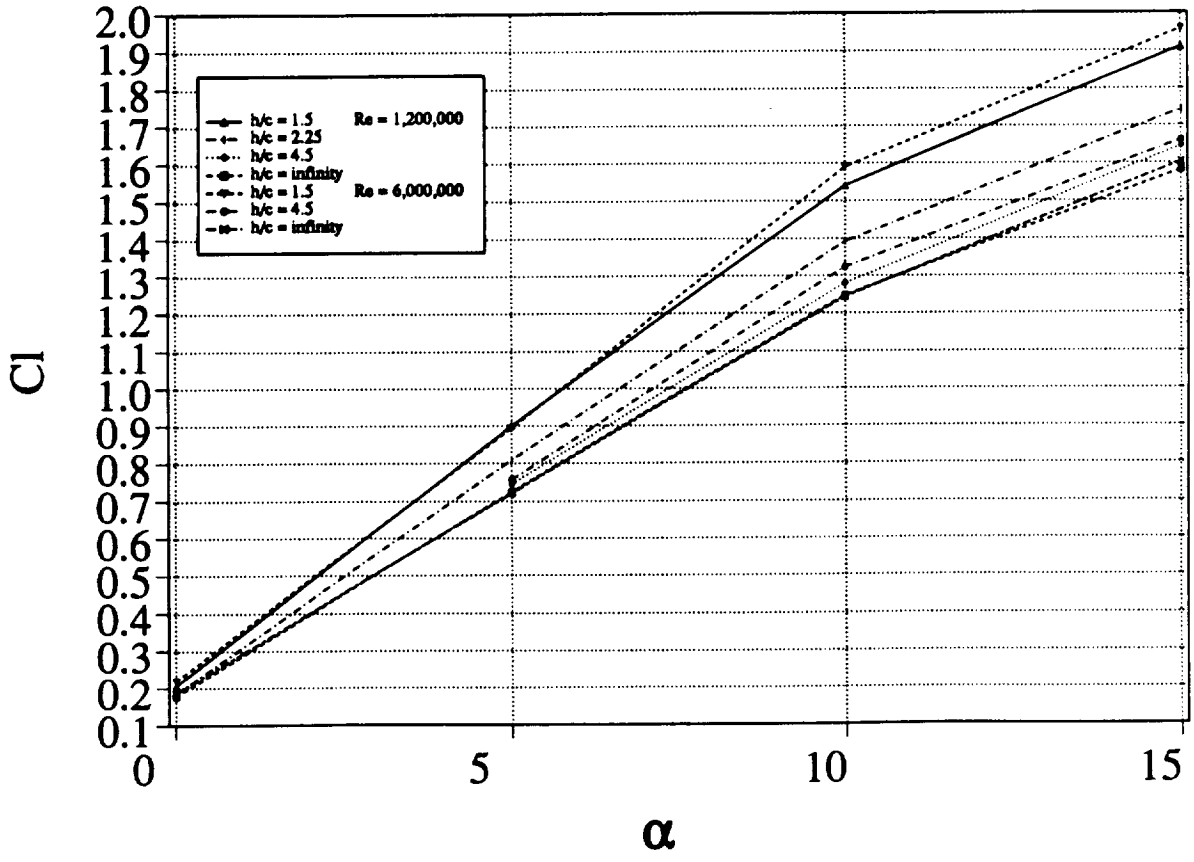

Figure 41: Lift Curves versus h/c

α (degrees)		0		5		10		15	
h/c	Re	$C_{d_{press}}$	$C_{d_{visc}}$	$C_{d_{press}}$	$C_{d_{visc}}$	$C_{d_{press}}$	$C_{d_{visc}}$	$C_{d_{press}}$	$C_{d_{visc}}$
1.5	1,200,000	.0030	.0075	.0090	.0079	.0252*	.0067	.0730	.0025
1.5	6,000,000	.0023	.0044	.0025*	.0051	.0134	.0046	.0718	.0019
2.25	1,200,000	.0032	.0068	.0050	.0077	.0087*	.0066	.0548	.0028
4.5	1,200,000	–	–	.0047	.0074	.0131	.0064	.0453	.0030
4.5	6,000,000	–	–	.0042	.0049	.0098	.0045	.0382	.0021
∞	1,200,000	.0026	.0074	.0065	.0077	.0158	.0066	.0443	.0032
∞	6,000,000	.0022	.0043	.0059	.0047	.0148	.0043	.0420	.0021

* significant error

Table 3: Pressure and Viscous Drag Coefficients

an important role in determining the flow field, there is no indication of any significant nonlinear behavior of lift coefficient with changes in h/c. Wind tunnel wall interference correction methods which are based on the idea of global corrections to freestream Mach number and angle of attack seem to be supported since lift curve slope is a function of Mach number in two dimensions and lift level is a function of angle of attack. But while the idea of ΔM and $\Delta\alpha$ may be correct, the effects which go into calculating these corrections need to be considered.

At the walls, increasing the Reynolds number shows no discernible trends (Figures 20, 25, 32, and 38) and in many cases has no effect at all on wall pressures, especially at the highest height to chord ratio. Figure 41 shows there to be some Reynolds number effects at the airfoil for $h/c =$ 4.5 even when wall pressures show none.

5.3 Drag

The drag can be broken down into that due to viscous forces, $C_{d_{visc}}$, and pressure forces, $C_{d_{press}}$, and these values are indicated in Table 3. Viscous drag is due to the viscous shearing forces and acts tangential to the solid surface. Pressure or form drag acts normal to a surface and is due to the displacement of the streamlines in the presence of separation. It is seen that the pressure drag makes a large contribution to

the total drag coefficient when the airfoil is at high angles of attack and is no longer a streamlined body.

Two major effects account for the variations in viscous drag behavior. The first effect causes an increase in $C_{d_{visc}}$ with decreasing height to chord ratio. The increase is due to the higher speed flow over the airfoil which increases the boundary layer edge velocity and at the same time the wall shear and, therefore, the skin friction. This is the dominant effect seen in all of the lower angle of attack, attached, constrained cases, where the viscous drag increases as the height to chord ratio is reduced (Figures 18, 19, 23, 24, 30, and 31).

The second, competing effect contributes to a decreased value of viscous drag with decreasing height to chord ratio. Since the velocities over the airfoil are increased as the height to chord ratio is decreased, the higher levels of lift promote separation which enlarges the recirculation region at the trailing edge. Increased amounts of reversed flow in the separated region decrease viscous drag by adding what can be considered as thrust. At fifteen degrees angle of attack the amount of separation is significant and the point of separation changes considerably with h/c (Figures 36 and 37). For the high angle of attack at both Reynolds numbers, this is the major influence on viscous drag, causing it to decrease with decreasing height to chord ratio. This is also the main effect for the attached, unconstrained, low Reynolds number runs, where the viscous drag trend reverses from that of the constrained cases and $C_{d_{visc}}$ increases because the amount of separation is reduced. For the high Reynolds number cases the trend does not reverse and the viscous drag further decreases in going from the constrained to unconstrained case.

In general at both Reynolds numbers, pressure drag follows the same trends as the viscous drag except at fifteen degrees angle of attack where it shows the opposite trend. Blockage effects of the boundary layer and larger recirculation regions substantially increase pressure drag so that form drag makes the overall drag show a marked increase as h/c is decreased and the separation point is moved upstream on the airfoil. In all cases the trailing edge separation is delayed at the higher Reynolds number.

The influences on drag are then the increased velocity over the airfoil which increases lift and viscous drag but also encourages separation which decreases lift and viscous drag but substantially increases pressure drag. Total drag coefficients generally increase with decreasing h/c, but are lowest for the highest height to chord ratio rather than the unconstrained case.

5.4 Code Characteristics

It should be noted that convergence to steady state was very slow for all cases. Because the code is explicit and high aspect ratio boundary layer cells make the equations stiff, thousands of iterations are needed to obtain a converged solution. Typically, 35,000 iterations were required on a sequence of grids for approximately four orders of magnitude reduction in the residual and a lift coefficient converged to within 1%. Total CPU time per run is approximately seven hours, depending on the size of the grid, using a single processor of a Cray YMP. CFL numbers based on monotonicity principles as high as 2.3 were used. The entire code is vectorized for increased speed on the Cray by "coloring" edges and faces so that loops with data dependencies are broken down into several nonrecursive loops. Solutions started from other solutions, *e.g.* when the height to chord ratio was reduced or the Reynolds number was increased, required approximately 10,000–15,000 iterations on the finest grid for reconvergence.

The convergence is especially slow for two reasons. First, the formulation is compressible and all of the solutions presented here are for small Mach number. Current algorithms developed for compressible flow based on wave propagation do not efficiently model the elliptic nature of low Mach number flow. The confined wind tunnel also contributed to convergence problems. Pressure waves reflect inside the tunnel, and even when they are damped with appropriate boundary conditions, they slow convergence and cause the solution to oscillate. Low frequency waves are the hardest to damp out and their presence is not indicated by the residual which only measures local, high frequency error. Low frequency pressure oscillations can be seen in Figure 32 on the walls behind the airfoil for $h/c = 1.5$. Although lift and viscous drag

were converged to within 1% for all cases, small changes in surface pressures produce large changes in the pressure drag. For the smaller height to chord ratios at higher angles of attack, the solutions often never did converge enough to give accurate values of pressure drag. This difficulty could be attributed to the surface pressure integrations, but the surface grids are fairly refined, especially at the leading edge due to the grid adaption. Similar convergence problems for nearly incompressible, confined flow have been reported on structured grids using implicit, compressible methods [17]. The unconstrained flow cases showed more monotonic convergence as did the supercritical cases.

The main reason for using the present code was its ability model complex geometries in anticipation of computing the flow about multielement airfoils. In its current form, though, it can only be considered a research tool.

Chapter 6

Conclusions

A method for computing wind tunnel flows has been developed using an unstructured grid Navier-Stokes computational fluid dynamics code. The code uses the Baldwin-Lomax algebraic turbulence model. For the unstructured grid, boundary layer profiles normal to the body are constructed using boundary geometry information. The grid generation process has been illustrated on a complex multielement airfoil geometry to show the benefits of an unstructured grid while still retaining some of the advantages offered by structured grids, namely the stretched quadrilateral boundary layer and wake cells. Special procedures are employed to handle these high aspect ratio cells during the triangulation process. Grid adaption was used to resolve various flow features and to speed up convergence to steady state. Using grid adaption on an initial coarse grid helps ease some of the difficulties of working with the highly stretched cells. The exit boundary condition is influential in wind tunnel flow computations, and without the advantage of experimental wind tunnel test data, freestream pressure was imposed at the outflow boundary.

The ability to model wind tunnel flows directly is useful for CFD validation, particularly turbulence models; wind tunnel wall correction methods development; and fundamental studies of flow physics. Results were presented of an investigation of the effect of wind tunnel wall proximity and Reynolds number on a single element airfoil model at low speed and four angles of attack up to stall. Decreasing the wind tunnel height to chord ratio was seen to increase both the lift and drag coefficients at

all angles of attack, although the drag coefficient also increased for the unconstrained cases from that of the $h/c = 4.5$ cases. Closer wind tunnel wall proximity and lower Reynolds number promoted earlier separation. Separation decreases viscous drag, but the larger extent of the boundary layer and recirculation region significantly increase pressure drag which then becomes the major contributor to total drag. For the subsonic cases considered, the results support the idea of Mach number and angle of attack corrections to wind tunnel data to obtain an equivalent unconstrained flow. For the attached flow cases, the lift curves remained linear but their slopes and levels of lift increased as the wind tunnel walls were moved in or as Reynolds number was increased.

The highest height to chord ratio of 4.5 does not simulate the unconstrained flow at any of the angles of attack investigated here as indicated by the airfoil pressure distributions or global aerodynamic parameters. Wind tunnel wall interference correction methods would be required for all cases. The effects which go into computing the corrections should include viscous phenomena for optimal accuracy, especially at higher angles of attack. Wall pressure plots did not always reflect Reynolds number effects at the airfoil. It seems doubtful that wind tunnel wall interference correction methods which use only wall pressure measurements could differentiate Reynolds number effects at the airfoil when no viscous modeling is included. Correction methods should therefore use airfoil pressures as well as wall measurements or include a viscous formulation in the numerical method.

Future work should focus on enhancements to speed up the code. Computation times for unstructured grid, explicit codes with multigrid have been demonstrated to approach the speed of equivalent structured, implicit codes [7]. The benefits of unstructured grids, including the ability to model complex flows and grid adaption to relevant flow features, make some additional time penalty worthwhile. Modifications to the Baldwin-Lomax turbulence model to include the ability to handle confluent boundary layers or a switch to a one or two equation model is also recommended. Changes to the algebraic model require being able to differentiate between boundary layers and overlying wakes so that separate length scales can be computed. Development of a porous wall boundary condition will allow investigation of porous wall

wind tunnels, although they are rarely used for the low Mach number flows considered here. Resolution of the wall boundary layer will distinguish the airfoil viscous effects from those due to the walls.

Bibliography

[1] Mokry, M., Chan, Y. Y., and Jones, D. J., "Two-Dimensional Wind Tunnel Wall Interference", *AGARDograph No. 281, AGARD-AG-281*, November 1983.

[2] Newman, P. and Barnwell, R., "Wind Tunnel Wall Interference Assessment/Correction", *NASA CP 2319*, January 1983.

[3] Celik, Z., "Flow Measurements of an Airfoil with Single Slotted Flap", *AIAA Paper 89-0533*, January 1989.

[4] Barth, T. and Jespersen, D., "The Design and Application of Upwind Schemes on Unstructured Meshes", *AIAA Paper 89-0366*, January 1989.

[5] Baldwin, B. and Lomax, H., "Thin Layer Approximation and Algebraic Turbulence Model for Separated Turbulent Flows", *AIAA Paper 78-0257*, January 1978.

[6] Rostand, P., "Algebraic Turbulence Models for the Computation of Two-Dimensional High Speed Flows Using Unstructured Grids", *ICASE Report 88-63*, November 1988.

[7] Mavriplis, D., "Euler and Navier-Stokes Computations for Two-Dimensional Geometries and Unstructured Meshes", *ICASE Report 90-3, NASA CR 181977*, January 1990.

[8] Agoropoulos, D. and Squire, L., "Interactions Between Turbulent Wakes and Boundary Layers", *AIAA Journal*, Vol. 26, No. 10, 1988, pp. 1194–1200.

[9] Cordova, J. and Barth, T., "Grid Generation for General Two-Dimensional Regions Using Hyperbolic Equations", *AIAA Paper 88-0520*, January 1988.

[10] Merriam, M., "A Fast, Robust Algorithm for Delauney Triangulation", *to be published*, NASA-Ames Research Center, 1989.

[11] Mavriplis, D., "Adaptive Mesh Generation for Viscous Flows Using Delauney Triangulation", *ICASE Report 88-47, NASA CR 181699*, August 1988.

[12] Dannenhoffer, J. and Baron, J., "Robust Grid Adaption for Complex Transonic Flows", *AIAA Paper 86-0495*, January 1986.

[13] Moretti, G., "A Physical Approach to the Numerical Treatment of Boundaries in Gas Dynamics", *NASA CP 2001*, October 1981.

[14] Kaynak, U. and Flores, J., "Advances in the Computation of Transonic Separated Flows over Finite Wings", *Computers and Fluids*, Vol. 17, No. 2, 1989, pp. 313–332.

[15] Rudy, D. and Strikwerda, J., "Boundary Conditions for Subsonic Compressible Navier-Stokes Calculations", *Computers and Fluids*, Vol. 9, 1981, pp. 327–338.

[16] Labrujère, T., Maarsingh, R., and Smith, J., "Wind Tunnel Wall Interference Considering Two-Dimensional High Lift Configurations", *Journal of Aircraft*, Vol. 23, No. 2, February 1986, pp. 118–125.

[17] Viegas, J., Rubesin, M., and MacCormack, R., "On the Validation of a Code and Turbulence Model Appropriate to Circulation Control Airfoil", *AGARD CP 437*, Vol 1, May 1988, pp. 6-1–6-21.